



1 **Pre-monsoon air quality over Lumbini, a world heritage site**  
2 **along the Himalayan foothills**

3 Dipesh Rupakheti<sup>1,2\*</sup>, Bhupesh Adhikary<sup>3</sup>, Puppala S. Praveen<sup>3</sup>, Maheswar Rupakheti<sup>4,5</sup>,  
4 Shichang Kang<sup>6,7\*</sup>, Khadak S. Mahata<sup>4</sup>, Manish Naja<sup>8</sup>, Qianggong Zhang<sup>1,7</sup>, Arnico K. Panday<sup>3</sup>,  
5 Mark G. Lawrence<sup>4</sup>

6 <sup>1</sup>Key Laboratory of Tibetan Environment Changes and Land Surface Processes, Institute of  
7 Tibetan Plateau Research, Chinese Academy of Sciences, Beijing 100101, China

8 <sup>2</sup>University of Chinese Academy of Sciences, Beijing 100049, China

9 <sup>3</sup>International Centre for Integrated Mountain Development (ICIMOD), Kathmandu, Nepal

10 <sup>4</sup>Institute for Advanced Sustainability Studies (IASS), Potsdam 14467, Germany

11 <sup>5</sup>Himalayan Sustainability Institute (HIMSI), Kathmandu, Nepal

12 <sup>6</sup>State Key Laboratory of Cryospheric Science, Cold and Arid Regions Environmental and  
13 Engineering Research Institute (CAREERI), Lanzhou 730000, China

14 <sup>7</sup>Center for Excellence in Tibetan Plateau Earth Sciences, Chinese Academy of Sciences, Beijing  
15 100085, China

16 <sup>8</sup>Aryabhata Research Institute of Observational Sciences (ARIES), Nainital, India

17

18 *\*Correspondence to:*

19 D. Rupakheti ([dipesh.rupakheti@itpcas.ac.cn](mailto:dipesh.rupakheti@itpcas.ac.cn)), S.C. Kang ([shichang.kang@lzb.ac.cn](mailto:shichang.kang@lzb.ac.cn))

20

21



## 22 Abstract

23 Lumbini, in southern Nepal, is a UNESCO world heritage site of universal value as the  
24 birthplace of Buddha. Poor air quality in Lumbini and surrounding regions is a great concern for  
25 public health as well as for preservation, protection and promotion of Buddhist heritage and  
26 culture. We present here results from measurements of ambient concentrations of key air  
27 pollutants (PM, BC, CO, O<sub>3</sub>) in Lumbini, first of its kind for Lumbini, conducted during an  
28 intensive measurement period of three months (April-June 2013) in the pre-monsoon season. The  
29 measurements were carried out as a part of the international air pollution measurement  
30 campaign; SusKat-ABC (Sustainable Atmosphere for the Kathmandu Valley - Atmospheric  
31 Brown Clouds). The ranges of hourly average concentrations were: PM<sub>10</sub>: 10.5 - 604.0 μg m<sup>-3</sup>,  
32 PM<sub>2.5</sub>: 6.1 - 272.2 μg m<sup>-3</sup>; BC: 0.3 - 30.0 μg m<sup>-3</sup>; CO: 125.0 - 1430.0 ppbv; and O<sub>3</sub>: 1.0 - 118.1  
33 ppbv. These levels are comparable to other very heavily polluted sites throughout South Asia.  
34 The 24-h average PM<sub>2.5</sub> and PM<sub>10</sub> concentrations exceeded the WHO guideline very frequently  
35 (94% and 85% of the sampled period, respectively), which implies significant health risks for the  
36 residents and visitors in the region. These air pollutants exhibited clear diurnal cycles with high  
37 values in the morning and evening. During the study period, the worst air pollution episodes  
38 were mainly due to agro-residue burning and regional forest fires combined with meteorological  
39 conditions conducive of pollution transport to Lumbini. Fossil fuel combustion also contributed  
40 significantly, accounting for more than half of the ambient BC concentration according to  
41 aerosol spectral light absorption coefficients obtained in Lumbini. WRF-STEM, a regional  
42 chemical transport model, was used to simulate the meteorology and the concentrations of  
43 pollutants. The model was able to reproduce the variation in the pollutant concentrations well;  
44 however, estimated values were 1.5 to 5 times lower than the observed concentrations for CO  
45 and PM<sub>10</sub> respectively. Regionally tagged CO tracers showed the majority of CO came from the  
46 upwind region of Ganges valley. The model was also used to examine the chemical composition  
47 of the aerosol mixture, indicating that organic carbon was the main constituent of fine mode  
48 PM<sub>2.5</sub>, followed by mineral dust. Given the high pollution level, there is a clear and urgent need  
49 for setting up a network of long-term air quality monitoring stations in the greater Lumbini  
50 region.

51



## 52 1. Introduction

53 The Indo-Gangetic plain (IGP) stretches over 2000 km encompassing a vast area of land in  
54 northern South Asia: the eastern parts of Pakistan, most of northern and eastern India, southern  
55 part of Nepal, and almost all of Bangladesh. The Himalayan mountains and their foothills stretch  
56 along the northern edge of IGP. The IGP region is among the most fertile and most intensely  
57 farmed region of the world. It is a heavily populated region with about 900 million residents or  
58 12% of the world's population. Four megacities - Lahore, Delhi, Kolkata, and Dhaka are located  
59 in the IGP region, with dozens more cities with populations exceeding one million. The region  
60 has witnessed impressive economic growth in recent decades but unfortunately it has also  
61 become one of the most polluted, and an air pollution 'hot spot' of local, regional and global  
62 concern (Ramanathan et al., 2007). Main factors contributing to air pollution in the IGP and  
63 surrounding regions include emissions from vehicles, thermal power plants, industries, biomass  
64 and fossil fuel used in cooking and heating activities, agricultural activities, crop residue burning  
65 and forest fires. Air pollution gets transported long distances away from emission sources and  
66 across national borders. As a result, the IGP and adjacent regions get shrouded with a dramatic  
67 annual buildup of regional scale plumes of air pollutants, known as Atmospheric Brown Clouds  
68 (ABC), during the long and dry winter and pre-monsoon seasons each year (Ramanathan and  
69 Carmichael, 2008). Figure 1 shows the mean aerosol optical depth (AOD) acquired with the  
70 MODIS instrument onboard TERRA satellite over South Asia for a period of December 2012-  
71 June 2013. Very high aerosol loading along the entire stretch of IGP reflects severity of air  
72 pollution over large area in the region.

73 Poor air quality continues to pose significant threat to human health in the region. In a new study  
74 of global burden of disease released recently, Forouzanfar et al. (2015) estimated that in 2013  
75 around 1.7 million people died prematurely in Pakistan, India, Nepal, and Bangladesh as a result  
76 of air pollution exposure, nearly 30% of global total premature deaths due to air pollution. Air  
77 pollution also affects precipitation (e.g. South Asian monsoon), agricultural productivity,  
78 ecosystems, tourism, climate, and broadly socio-economic and national development goals of the  
79 countries in the region (Burney and Ramanathan, 2014; Shindell, 2011; Ramanathan and  
80 Carmichael, 2008). It has also been linked to intensification of cold wave and winter fog in the  
81 IGP region over recent decades (Lawrence and Lelieveld, 2010 and references therein; Safai et



82 al., 2009; Ganguly et al., 2006). Besides high levels of aerosol loading as shown in Fig. 1, Indo-  
83 Gangetic plains also have very high levels of ground level ozone or tropospheric ozone ( $O_3$ )  
84 (e.g., Ramanathan and Carmichael (2008)). It is a toxic pollutant to plant and human health, and  
85 a major greenhouse gas (IPCC, 2013; Shindell, 2011; Mohnen et al., 1993). South Asia, in  
86 particular IGP region, has been projected to be most ozone polluted region in world by 2030  
87 (Stevenson et al., 2006). Majority of crop loss in different parts of the world results from effects  
88 of ozone on crop health and productivity (Shindell, 2011). For example, Burney and Ramanathan  
89 (2014) reported a significant loss in wheat and rice yields in India from 1980 to 2010 due to  
90 direct effects of black carbon (BC) and ozone ( $O_3$ ). BC and  $O_3$  are two key short-lived climate  
91 pollutants (SLCP). Because of the IGP's close proximity to the Himalaya-Tibetan plateau region,  
92 this once relatively clean region, is now subjected to increasing air pollution transported from  
93 regions such as the IGP, which can exert additional risks to human health and sensitive  
94 ecosystems in the mountain region (e.g., (Lüthi et al., 2015; Marinoni et al., 2013; Duchi et al.,  
95 2011). Studies have shown elevated BC loading over the Himalaya-Tibetan region results in  
96 additional atmospheric warming which combined with BC deposition on snow and ice leads to  
97 accelerated melting of the snow and glaciers (Shindell, 2011; Xu et al., 2009; Ramanathan and  
98 Carmichael, 2008). Air pollution transport pathways to Himalayas are still not yet fully  
99 understood.

100 Air pollution can also damage the built environment and cultural and archeological heritages  
101 (Brimblecombe, 2003). Monuments and buildings made with stones are vulnerable to air  
102 pollution damage (Brimblecombe, 2003; Gauri and Holdren, 1981). Sulfur dioxide, which forms  
103 sulfuric acid upon reaction with water is the most harmful substance for the monuments as it can  
104 corrode and damage them (Baedecker et al., 1992; Gauri and Holdren, 1981). Indo-Gangetic  
105 plains are rich in archeological, cultural and historical sites and monuments and many of them  
106 are inscribed as UNESCO World Heritage Site. For example, among many other such sites in  
107 IGP are the Archaeological Ruins at Moenjodaro (Pakistan), Taj Mahal in Agra and Mahabodhi  
108 Temple Complex in Bodh Gaya (India), Lumbini (Nepal), and ruins of the Buddhist Vihara at  
109 Paharpur (Bangladesh) (World Heritage List; UNESCO, website: <http://whc.unesco.org/en/list>).  
110 The Taj Mahal is one of the seven wonders of the modern world and India's greatest landmark.  
111 Starting in 1970s, there have been observations of brownish/yellowish tone on its shiny



112 white marble façade, and the primary suspect of discoloration was heavy air pollution from  
113 industries and traffic that grew around the monument site in Agra over the past decades. At the  
114 end of the last century, the government of India realized the growing problem and started a  
115 program to save the monument. It introduced measures to cut back pollution, as well as set up  
116 stations around the monument to monitor air quality around the clock. A recent study has  
117 reported that deposition of light absorbing aerosol particles (black carbon, brown carbon) and  
118 dust is responsible for its discoloration (Bergin et al., 2015).

119 Lumbini, located near the northern edge of the central Ingo-Gangetic plain, is famous as the  
120 birthplace of the Lord Buddha. Lumbini is a UNESCO world heritage site of outstanding  
121 universal value to humanity, inscribed in the UNESCO list since 1997. The site, with valuable  
122 archaeological remains of the Buddhist *Viharas* (monasteries) and *Stupas* (memorial shrines), as  
123 well as modern temples and monasteries, is a center of attraction and visited by hundreds of  
124 thousands of pilgrims, scientists, scholars, yogis, and tourists every year. Over recent years, there  
125 is increasing concern about poor air quality in Lumbini and the surrounding region. There is no  
126 surface monitoring of air quality in Lumbini.

127 As a first attempt to understand air quality in Lumbini, we carried out continuous measurements  
128 of ambient concentrations of key air pollutants (particulate matter, black carbon, carbon  
129 monoxide, ozone) and other auxiliary measurements (Aerosol optical depth – not discussed on  
130 the present study, meteorological parameters) during an intensive measurement period of three  
131 months (April-June) in the year 2013. These are the first reported measurements for Lumbini. A  
132 regional chemical transport model called Sulfur Transport and dEposition Model (STEM) was  
133 used to simulate the variations of meteorological parameters and air pollutants during the  
134 observation period. Regionally tagged CO tracers were used to identify emission source regions  
135 impacting pollutant concentration observed at Lumbini. Satellite data has also been used to  
136 understand the high pollution events during the monitoring period. These measurements were  
137 carried out as a part of the SusKat-ABC international air pollution measurement campaign (*M.*  
138 *Rupakheti, manuscript in preparation for ACPD*) jointly led by the International Centre for  
139 Integrated Mountain Development (ICIMOD), Kathmandu, Nepal and Institute for Advanced  
140 Sustainability Studies (IASS), Potsdam, Germany.



## 141 2. Experimental set up

### 142 2.1 Sampling site

143 The Lumbini measurement site (27°29.387' N, 83°16.745' E, elevation: ~100 m above sea level)  
144 is located at the premise of the Lumbini International Research Institute (LIRI), a Buddhist  
145 library in Lumbini. Lumbini lies in the Nepal's southern lowland plain or *Terai* region, termed as  
146 "bread basket of Nepal" due to the availability of very fertile land suitable for crop production,  
147 which forms the northern edge of the Indo-Gangetic Plains (IGP). 25 km north of Lumbini the  
148 foothills begin, while the main peaks of the Himalayas are 140 km to the north. The remaining  
149 three sides are surrounded by flat plain land of Nepal and India. The site is only about 8 km from  
150 the Nepal-India boarder in the south. A three storied 10 m tall water tower was used as the  
151 platform for the automatic weather station (AWS) whereas remaining instruments were placed  
152 inside a room near the base of the tower. Figure 2 shows the location of Lumbini, the Kenzo  
153 Tange Master Plan area of the Lumbini development project, and the sampling tower. An  
154 uninterrupted power back up was set up in order to assure the regular power supply even during  
155 hours with scheduled power cuts during the monitoring period. The nearby premises of the  
156 monitoring site consist of the LIRI main office and staff quarters. Further away is a museum, a  
157 local bus park for the visitors to Lumbini, the office of the Lumbini Development Trust,  
158 monasteries, and thinly forested area with grassland within the master plan area. Outside of the  
159 master plan area lie vast area of agricultural fields, village pockets, and several brick kilns and  
160 cement industries. A local road (black topped), that cuts through the master plan area, lies about  
161 200 m north of the sampling site and experiences intermittent passing of vehicles. According to  
162 the Ministry of Culture, Tourism and Civil Aviation of Nepal over 130 thousand tourists  
163 (excluding Nepalese and Indian citizens) visited the Lumbini area in 2014  
164 (<http://tourism.gov.np/en>).

### 165 2.2 Monitoring Instruments

166 The summary of instruments deployed in Lumbini is presented in Table 1. They monitored  
167 ambient concentrations of various air pollutants and local meteorological parameters  
168 continuously during the sampling period of about two and half months. All data were collected in  
169 Nepal Standard Time (NST) which is GMT +05:45 hour. PM<sub>10</sub>, PM<sub>2.5</sub> and PM<sub>1</sub> mass



170 concentrations were monitored continuously with GRIMM EDM164 (GRIMM Aerosol Technik,  
171 Germany), reporting data every 5 min. The instrument uses the light scattering at 655 nm to  
172 derive mass concentrations. More description on the technical aspects of the instrument can be  
173 found on the manufacturer's website ([http://wiki.grimm-aerosol.de/index.php?title=ENVIRO-](http://wiki.grimm-aerosol.de/index.php?title=ENVIRO-EDM164)  
174 EDM164). The EDM164 used in this study was a newly purchased instrument which was  
175 calibrated at the factory of the GRIMM Aerosol Technik in Germany before it was deployed at  
176 Lumbini. Similarly, aerosol light absorptions at 7 wavelengths (370, 470, 520, 590, 660, 880,  
177 950 nm) were measured continuously with an Aethalometer (Model AE-42, Magee Scientific,  
178 USA), averaging and reporting data every 5 min. AE-42 was operated at a flow rate of 5 l min<sup>-1</sup>.  
179 As described by the manufacturer, ambient BC concentration is derived from light absorption at  
180 880 nm using a specific mass absorption cross section. To obtain BC concentration in Lumbini,  
181 we used a specific mass absorption cross-section value of 8 m<sup>2</sup> g<sup>-1</sup> for the 880 nm channel.  
182 Similar value has been previously used for BC measurement in the Indo-Gangetic plain (Praveen  
183 et al., 2012). Optical measurement by filter-based absorption photometers, such as the  
184 Aethalometer, suffer from measurement artifact known as filter loading effect which must be  
185 taken into account and corrected for while deriving ambient BC concentrations. We used  
186 correction method suggested by Schmid et al. (2006) which was also used by Praveen et al.  
187 (2012) for BC measurements at a rural site in the Indo-Gangetic plain. Surface ozone (O<sub>3</sub>)  
188 concentration was measured continuously with an ozone analyzer (Model 49i, Thermo Scientific,  
189 USA), reporting data every minute. It utilizes UV (254 nm wavelength) photometric technology  
190 to measure ozone concentration in ambient air. CO analyzer (Model 48i, Thermo Scientific,  
191 USA) was used to monitor ambient CO concentrations, recording data every minute. The CO  
192 analyzer is based on the principle that CO absorbs infrared radiation at the wavelength of 4.6  
193 microns. The ambient air was drawn through 6-micron pore size SAVILLEX 47 mm filter at the  
194 inlet in order to remove the dust particles before sending air into the CO and O<sub>3</sub> analyzers using a  
195 Teflon tube. The filters were replaced every 7-10 days depending on particle loading, based on  
196 manual inspection. Both CO and O<sub>3</sub> analyzers were new instruments, freshly calibrated at the  
197 factory before deploying them in Lumbini. The CO instrument was set to auto-zero at a regular  
198 interval of 6 hours. Local meteorological parameters (temperature, relative humidity, wind  
199 speed, wind direction, precipitation, and global solar radiation) were monitored with an



200 automatic weather station (AWS) (Campbell Scientific, Loughborough, UK), recording data  
201 every minute.

### 202 **2.3 Regional chemical transport model**

203 Aerosol and trace gas distributions were simulated using a regional chemical transport model.  
204 Sulfur Transport and dEposition Model (STEM), a 3D eulerian model, that has been used  
205 extensively in the past to characterize air pollutants in South Asian region was used to interpret  
206 observations at Lumbini (Kulkarni et al., 2015; Adhikary et al., 2007). The Weather Research  
207 and Forecasting (WRF) model (Skamarock et al., 2008) version 3.5.1 was used to generate the  
208 required meteorological variables necessary for simulating pollutant transport in STEM. The  
209 model domain was centered at 24.94° N latitude and 82.55° E longitude covering a region from  
210 3.390° N to 43.308° N latitudes and 34.880° E to 130.223° E longitudes. The model has 425×200  
211 horizontal grid cells with grid resolution of 25×25 km and 41 vertical layers with top of the  
212 model set at 50 mbar. The WRF model was run from November 1, 2012 to June 30, 2013.  
213 However, for this study, modeled data only from April to June 2013 have been used. The WRF  
214 model was initialized with FNL data available from NCAR/UCAR site  
215 (<http://rda.ucar.edu/datasets/ds083.2/>).

216 The tracer version of the STEM model provides mass concentration of sulfate, BC (hydrophilic  
217 and hydrophobic), Organic carbon (OC), sea salt (fine and coarse mode), dust (fine PM<sub>2.5</sub> and  
218 PM<sub>10</sub>), CO (biomass and anthropogenic) and region tagged CO tracers. STEM model domain  
219 size, resolution and projection are those of the WRF model. Details about tracer version of the  
220 STEM model is outlined elsewhere (Kulkarni et al., 2015; Adhikary et al., 2007).  
221 Anthropogenic emission of various pollutants (CH<sub>4</sub>, CO, SO<sub>2</sub>, NO<sub>x</sub>, NMVOC, NH<sub>3</sub>, PM<sub>10</sub>,  
222 PM<sub>2.5</sub>, BC and OC) used in this analysis were taken from the EDGAR-HTAP\_v2  
223 ([http://edgar.jrc.ec.europa.eu/htap\\_v2/index.php?SECURE=123](http://edgar.jrc.ec.europa.eu/htap_v2/index.php?SECURE=123)). Emission inventory were  
224 developed for the year 2010 gridded at the spatial resolution of 0.1°×0.1°. Open biomass burning  
225 emissions on a daily basis during the simulated period were taken from data obtained from the  
226 FINN model (Wiedinmyer et al., 2011). As with the WRF model, the STEM model was run from  
227 November 2, 2012 to June 30, 2013 however, data presented here are only during the intensive  
228 field campaign period.



## 229 3 Results and discussions

### 230 3.1 Meteorology

#### 231 3.1.1 Time series of local meteorological parameters

232 Hourly average time series of various meteorological parameters viz. precipitation in  $\text{mm hr}^{-1}$   
233 (Prec), relative humidity in % (RH), temperature in  $^{\circ}\text{C}$  (T), wind direction in degree (WD) and  
234 wind speed in  $\text{m s}^{-1}$  (WS) during the monitoring period are shown in Figure 3. Meteorological  
235 parameters were obtained with the sensors at the height of  $\sim 12$  m from the ground. Moreover,  
236 meteorology results from simulations using a 3D model have been used to compare with the  
237 observations, and to fill the data gaps. Precipitation data was derived from TRMM satellite  
238 (TRMM\_3B42\_007 at a horizontal resolution of  $0.25^{\circ}$ ) from the Giovanni platform  
239 (<http://giovanni.gsfc.nasa.gov/giovanni/>) as the rain gauge malfunctioned during the sampling  
240 period.

241 Average observed wind speed during the study period was  $2.4 \text{ m s}^{-1}$ , with hourly values ranging  
242 between  $0.03 - 7.4 \text{ m s}^{-1}$  whereas from the WRF model average wind speed was found to be  $3.2$   
243  $\text{m s}^{-1}$  (range:  $0.06 - 11.1 \text{ m s}^{-1}$ ). Comparison of the model output data with observation shows  
244 that the model adequately captures wind speed to study pollutant transport. Diurnal variation of  
245 observed hourly average wind speed suggested that wind speeds were lower during nights and  
246 mornings while higher wind speed prevailed during day time, with average winds  $> 3 \text{ m s}^{-1}$  up to  
247  $\sim 3.3 \text{ m s}^{-1}$  between 09:00-13:00 local time (Supplementary materials, Figure S1, upper panel).  
248 High speed strong winds ( $> 4 \text{ m s}^{-1}$ ) were from the NW direction during the month of April  
249 which later switched to almost opposite direction, i.e., SE direction from the month of May  
250 onwards. Figure 4 shows the monthly wind rose plot (using WRPLOT view from the Lakes  
251 Environmental, <http://weblakes.com/>). Average observed temperature for the sampling period  
252 until the sensor stopped working (on 8<sup>th</sup> May, 2013, i.e., for 38 days) was  $28.1^{\circ}\text{C}$ , with a  
253 minimum value recorded to be  $16.5^{\circ}\text{C}$  whereas the maximum was  $40^{\circ}\text{C}$ . Average T from the  
254 model, during same period, was  $31^{\circ}\text{C}$  with values ranging between  $19 - 40^{\circ}\text{C}$ . The model  
255 captures the synoptic variability of temperature and is mostly within the range of daily values.  
256 However, the model has a high bias and does not capture daily minimum temperature values. For  
257 the same period (until the sensor stopped working), the average (observed) RH was  $\sim 50\%$



258 (ranging from 10.5 to 97.5%) whereas the model showed the average RH to be ~ 23% (same  
259 period as observation) with values ranging between 6 to 78%. RH values are highly  
260 underestimated by the model however; the synoptic scale variability is captured by the model.  
261 Discrepancy on model results might have occurred due to various factors inherently uncertain in  
262 a weather model. However, we believe that modeled data is vital for understanding pollutant  
263 transport in an area where observation data are non-existent or are incomplete.

### 264 3.1.2 Synoptic scale winds during pre-monsoon

265 The monthly mean synoptic wind for the month of April, May and June is presented in Figure 5.  
266 NCEP/NCAR reanalysis monthly data of winds at 1000 mbar were used to study the wind  
267 pattern. The red dot in the figure indicates the location of Lumbini. NCEP/NCAR data showed  
268 the dominance of calm winds over the measurement site. Similar type of wind directions were  
269 observed over Kanpur, India, also in the IGP, during the pre-monsoon season (Srivastava et al.,  
270 2011).

271

## 272 3.2 Time series of air pollutants

### 273 3.2.1 General overview

274 Figure 6 shows hourly averaged time series of both observed and modeled PM<sub>10</sub>, PM<sub>2.5</sub>, BC, CO  
275 and O<sub>3</sub> observed at Lumbini during the study period. In this section, results have been discussed  
276 based upon the observation datasets only. Section 3.2.3 will discuss model comparison and  
277 interpretation.

278 *Both PM fractions:* PM<sub>10</sub> and PM<sub>2.5</sub> showed similar temporal behavior. Observed hourly average  
279 PM<sub>10</sub> concentrations ranged between 10.5-603.9  $\mu\text{g m}^{-3}$  with an average of  $128.9\pm 91.9 \mu\text{g m}^{-3}$   
280 whereas PM<sub>2.5</sub> concentrations ranged between 6.1 and 272.2  $\mu\text{g m}^{-3}$  with an average of  $53.1\pm 35.1$   
281  $\mu\text{g m}^{-3}$  during the sampling period. In addition to this, average PM<sub>1</sub> concentration was  $35.8\pm 25.6$   
282  $\mu\text{g m}^{-3}$  with the concentrations ranging between 3.6 to 197.6  $\mu\text{g m}^{-3}$ . PM<sub>1</sub> concentration has not  
283 been discussed in this study. The observed 24 hour average particulate matter concentrations  
284 (PM<sub>2.5</sub> and PM<sub>10</sub>) were found frequently higher than the WHO prescribed guidelines for PM<sub>2.5</sub>  
285 ( $25 \mu\text{g m}^{-3}$ ) and PM<sub>10</sub> ( $50 \mu\text{g m}^{-3}$ ), (WHO, 2006) – PM<sub>2.5</sub>: 94% and PM<sub>10</sub>: 85% of the



286 measurement period of 53 days. Similarly, BC concentrations during the measurement period  
287 ranged between 0.3-29.9  $\mu\text{g m}^{-3}$  with a mean ( $\pm$ SD) value of 4.9 ( $\pm$ 3.8)  $\mu\text{g m}^{-3}$ . The lowest  
288 concentration was observed during a rainy day (21-22 April) whereas the highest concentration  
289 was observed during a period of forest fire (detailed in Section 3.4). BC concentrations in  
290 Lumbini during pre-monsoon months are lower compared to BC concentrations observed in the  
291 Kathmandu Valley because of high number of vehicles plying on the street, brick kilns and other  
292 industries in Kathmandu valley (Putero et al., 2015; Sharma et al., 2012).

293 CO concentrations ranged between 124.9-1429.7 ppbv with an average value of 344.1 $\pm$ 160.3  
294 ppbv. CO concentration observed in Lumbini is lower than that of Mohali, Western India where  
295 the average concentration was 566.7 ppbv during pre-monsoon season due to intense biomass  
296 and agro-residue burning over the region (Sinha et al., 2014). Temporal variation of CO  
297 concentrations is similar to that of BC as both of these species are emitted during incomplete  
298 combustion of fuel. BC to CO ratio in Lumbini was found to be different from that observed at  
299 other urban and rural sites and those affected by forest fire/biomass burning. However, a sub-  
300 urban site, Pantnagar, in IGP also observed similar BC to CO ratio (Joshi et al., 2016) as  
301 observed in Lumbini. There was a very strong correlation ( $r > 0.9$ ) between BC and CO  
302 (Supplementary material, Figure S2), indicating likely common sources of emission for both  
303 pollutants. The hourly averaged observed ozone concentration ranged between 1.0 and 118.1  
304 ppbv with a mean value of 46.6 $\pm$ 20.3 ppbv during the sampling period. The 8-hr maximum O<sub>3</sub>  
305 concentration exceeded WHO guidelines of 100  $\mu\text{g m}^{-3}$  (WHO, 2006) during 88% of the  
306 measurement period. Our results clearly indicate that the current pollution levels in Lumbini is of  
307 great concern to health of the people living in the region as well as over a million visitors who  
308 visit Lumbini, as well as ecosystems, particularly agro-ecosystem, especially in warm and sunny  
309 pre-monsoon months.

### 310 3.2.2 Comparison with other south Asian sites

311 Past studies near this site have been focused on the cities like Kathmandu (Putero et al., 2015;  
312 Sharma et al., 2012; Ram et al., 2010; Panday and Prinn, 2009) and Kanpur (Ram et al., 2010)  
313 and agro-residue burning dominated regions of IGP (Rastogi et al., 2016; Sinha et al., 2014;  
314 Sarkar et al., 2013) or a remote mountain location in India (Naja et al., 2014). In order to put our



315 results in perspective, pollution levels observed in Lumbini have been compared with the  
316 observations from other sites in the region and are presented in Table 2. Very high aerosol  
317 loading is observed in South Asia during pre-monsoon, mostly over the IGP region  
318 (Supplementary materials, Figure S3).  $PM_{2.5}$  concentration in Lumbini have been found to be  
319 lower than the megacity like Delhi (Bisht et al., 2015) and north-western IGP regions (Sinha et  
320 al., 2014) due to higher level of emissions (from traffic and biomass burning respectively) over  
321 those regions. BC concentrations observed in Lumbini during pre-monsoon season was lower  
322 than the urban Asian cities like Kathmandu (Putero et al., 2015) and Delhi (Bisht et al., 2015),  
323 slightly higher than in Kanpur but high compared to the remote locations in the region. BC  
324 observed at Lumbini was higher by a factor of  $\sim 6$  and  $\sim 4.5$  compared to that at Mt. Abu, India  
325 (Das and Jayaraman, 2011) and near the base of Mt. Everest, Nepal (Marinoni et al., 2013)  
326 respectively. Regarding CO, concentration in Lumbini was  $\sim 1.5$ -5 times lower than other urban  
327 locations in India (Gaur et al., 2014; Sinha et al., 2014). However, Lumbini CO concentrations  
328 are  $\sim 2.3$ -2.6 times higher than nearby remote location such as Mt. Abu (Naja et al., 2003).  
329 Average  $O_3$  concentrations, over sampling period, in Lumbini were found to be higher than the  
330 cities like Kathmandu (Putero et al., 2015). However, ozone concentrations higher than that  
331 observed at Lumbini were reported at nearby city of Kanpur during pre-monsoon season (Gaur et  
332 al., 2014). Interestingly ozone concentrations higher than that at Lumbini were observed in the  
333 Mt. Everest region. Uplift of the polluted air masses (Marinoni et al., 2013), stratospheric  
334 intrusion (Cristofanelli et al., 2010) and even the regional or long-range transport of the air  
335 pollutants (Bonasoni et al., 2010) might have contributed for the higher ozone concentration over  
336 the Everest region, resulting in higher  $O_3$  concentration compared to Lumbini.

### 337 3.2.3 Observation-model inter-comparison

338 Chemical transport models provide insight to observed phenomena; however, interpretation has  
339 to take into account model performance before arriving at any conclusion. This section describes  
340 pollution concentrations simulated by the WRF-STEM model. A comparison of model calculated  
341 average concentration along with the minimum and maximum concentrations of various  
342 pollutants (with observation) is shown in Table 3. The model based concentrations used here are  
343 instantaneous values for every third hour of the day. Regarding  $PM_{2.5}$  and  $PM_{10}$ , the model  
344 simulated average concentration was  $17.3 \pm 6.7$  ( $1.9$ - $48.3$ )  $\mu g m^{-3}$  and  $25.4 \pm 12.9$  ( $2.1$ - $68.8$ )  $\mu g m^{-3}$



345 <sup>3</sup>, respectively. The model estimated values were lower by the factor of 3 and 5 respectively than  
346 the observed concentrations. Similarly, average CO concentration was  $255.7 \pm 83.5$  ppbv, ranging  
347 between 72.2–613.1 ppbv, with average model CO  $\sim 1.35$  times lower than observed. BC  
348 concentrations ranged between 0.4–3.7  $\mu\text{g m}^{-3}$  with a mean value of  $1.8 \pm 0.7$   $\mu\text{g m}^{-3}$  for a period  
349 of 1<sup>st</sup> April–15<sup>th</sup> June 2013. The average model BC concentration was  $\sim 2.7$  times lower than the  
350 observed BC. Previous study using the STEM model over Kathmandu valley showed the model  
351 was able to capture annual BC mean value but completely missed the concentrations during pre-  
352 monsoon and post monsoon period (Adhikary et al., 2007). Similar behavior is seen this time for  
353 CO where the model misses the peak values but reasonably captures CO concentration after mid-  
354 May. Even though the model calculated values are lower in the present study, the model captures  
355 the synoptic variability fairly well for all the pollutants compared. STEM model performance can  
356 be significantly improved via better constraining anthropogenic emissions inventory, emissions  
357 of open biomass burning (natural and anthropogenic) and improvements in meteorological  
358 output from WRF amongst many other uncertainties inherent in regional chemical transport  
359 model. This activity is beyond the scope of this current paper although the improvements are  
360 underway for all these sectors.

### 361 **Diurnal variations of air pollutants and boundary layer height**

362 In the emission source region, diurnal variations of primary pollutants provide information about  
363 the time dependent emission activities (Kumar et al., 2016). Figure 7 shows the diurnal variation  
364 of hourly averaged concentrations of various pollutants measured during the sampling period.  
365 Primary pollutants like PM<sub>10</sub>, CO and BC all showed typical characteristics of an urban  
366 environment, i.e., diurnal variation with a morning and an evening peak. However, Lumbini data  
367 shows higher concentrations in the evenings compared to morning hours. Elevated  
368 concentrations can be linked to morning and evening cooking hours for BC and CO where  
369 emission inventory show that residential sector has significant contribution. However,  
370 explanation for elevated evening concentration compared to morning needs further investigation.  
371 Increase in the depth of boundary layer, reduction in the traffic density on the roads, absence of  
372 open biomass burning during mid-day and increasing wind speed often contribute to the  
373 dispersion of pollutants resulting in lower concentration during afternoon. Diurnal variation of  
374 wind direction (Supplementary information, Figure S1, lower panel) shows the dominance of



375 wind coming from south (mainly during the month of May and till mid-June). Morning and  
376 evening period experienced the winds coming from the southeast direction while the winds were  
377 predominantly from southwest direction during late afternoon. Increase in CO concentrations in  
378 the evening hours might be due to transport of higher levels of CO emissions from source  
379 regions upwind of Lumbini which along with the local emissions gets trapped under lower  
380 Planetary Boundary Layer (PBL) heights in evening and night time. Ozone concentration was  
381 lowest in the morning before the sunrise and highest in late afternoon around 15:00 PM after  
382 which concentrations started declining, exhibiting a typical characteristic of a polluted urban site.  
383 Photo-dissociation of accumulated NO<sub>x</sub> reservoirs (like HONO) provides sufficient NO  
384 concentration leading to the titration of O<sub>3</sub> resulting in minimum O<sub>3</sub> just before sunrise (Kumar  
385 et al., 2016). The PBL height (in meters (m)) was obtained from the model as observations were  
386 not available. Figure 8 shows the diurnal variation of the model derived PBL height. The study  
387 period average PBL height over Lumbini was ~ 910 m (ranging between 24.28 and 3807 m  
388 observed at 06:00 and 15:00 h respectively). As the pre-monsoon month advances, PBL height  
389 also increased. The monthly average PBL height was 799 m, 956 m and 1014 m respectively  
390 during the month of April, May and (1<sup>st</sup>-15<sup>th</sup>) June. Over the IGP region, PBL height is deeper  
391 during the pre-monsoon compared to monsoon (Patil et al., 2014), post-monsoon (Hegde et al.,  
392 2009) and winter (Badarinath et al., 2009) seasons. The fluctuations of PBL height correspond  
393 well with the diurnal variation of the pollutants like BC, CO and PM with the period of lower  
394 boundary height experiencing higher pollution concentration.

### 395 **3.3 Influence of forest fires on Lumbini air quality**

#### 396 **3.3.1 Identification of forest fire influence over large scale using in-situ observations** 397 **satellite and model data**

398 Forest fires and biomass burning (mostly agro-residue burning in large scale) are common over  
399 the South Asia and the IGP region during pre-monsoon season. North Indo-Gangetic region is  
400 characterized by fires even during the monsoon and post-monsoon season (Kumar et al., 2016;  
401 Putero et al., 2014). These activities influence air quality not only over nearby regions but also  
402 get transported towards high elevation pristine environments like Everest (Putero et al., 2014)  
403 and Tibet (Cong et al., 2015a; 2015b). So, one of the main objectives of this study was to



404 identify the influence of open burning on Lumbini air quality. Average wind speed during the  
405 whole measurement period was  $2.4 \text{ m s}^{-1}$ . Based on this data, open fire counts within the grid  
406 size of  $200 \times 200 \text{ km}$  centering over Lumbini was used for this analysis assuming that the  
407 emissions will take a maximum period of one day to reach our monitoring site. Forest fire counts  
408 were obtained from MODIS satellite data product called Global Monthly Fire Location Products  
409 (MCD14ML). More on this has already been described by Putero et al. (2014). Figure 9 shows  
410 the daily average in-situ CO, BC, aerosol absorption Ångstrom exponent (AAE) which is derived  
411 from Aethalometer data and daily open fire count within the specified grid. The green box in the  
412 figure is used to show two outstanding events with the elevated BC and CO concentrations  
413 observed during the monitoring period. The first peak was observed during 7-9 April and second  
414 peak during 3-4 May, 2013. Two pollutants having biomass burning as the potential primary  
415 source: BC and CO were taken in consideration. AAE values higher during these two events ( $\sim$   
416 1.6) are also an indication of presence of BC of biomass burning origin. Ground based TSP  
417 sampling also showed higher concentration of biomass burning tracer (potassium or  $\text{K}^+$ ) in  
418 Lumbini during the pre-monsoon season comparing to other seasons of the year (*L. Tripathee,*  
419 *personal communication*). But, to our expectation, we could not observe any significant  
420 influence of forest fire within the specified grid (or the influence of local forest fire on the air  
421 quality over Lumbini was not observed). Therefore, a wider area, covering South and Southeast  
422 Asian regions, was selected for the forest fire count. Figure 10 (A-B) shows the active fire  
423 hotspots from MODIS, over the region, during the peak events which shows the first peak  
424 occurred due to the forest fire over the eastern India region whereas the second peak was  
425 influenced by the forest fire over western IGP region. Moreover, in order to strengthen our  
426 hypothesis, we have utilized satellite data products for various gaseous pollutants like CO and  
427  $\text{NO}_2$  (Atmospheric Infrared Sounder (AIRS) for CO and Ozone Monitoring Instrument (OMI) for  
428  $\text{NO}_2$  both obtained from Giovanni platform). Figure 10 (C-H) shows the daytime total column  
429 CO before, during and after occurrence of two events (peaks) as stated earlier. Atmospheric  
430 Infrared Sounder (AIRS) satellite with daily temporal resolution and  $1^\circ \times 1^\circ$  spatial resolution  
431 have been utilized to understand the CO concentration over the area. CO concentration over  
432 Lumbini during both of the peaks confirmed the role of open fires on either sides of the IGP  
433 region for elevated concentration of CO over Lumbini. To further strengthen our finding, the aid  
434 of wind rose plot of local wind speed and direction was taken. Figure 10 (I-J) represent the wind



435 rose plot only for these two events respectively. Wind rose plots also confirm the wind blowing  
436 from those two forest fire regions affected the air quality in Lumbini region. Figure10 (K) shows  
437 model biomass CO peak coincident with observed CO. Although the magnitudes are different,  
438 the timing of the peaks is well captured by the model. However, satellite based open fire  
439 detection also has limitation as it does not capture numerous small fires that are prevalent over  
440 south Asia which usually burn out before the next satellite overpass. More research is needed to  
441 assess the influence of these small fires on regional air quality.

442 In a separate analysis (not shown here), elevated O<sub>3</sub> concentration during these two events were  
443 also observed. Average O<sub>3</sub> concentration before, during and after the events were found to be  
444 46.2±20.3 ppbv, 53.5±31.1 ppbv and 50.3±20.9 ppbv respectively (Event-I) whereas it was  
445 found to be 54.8±23.8 ppbv, 56.7±35 ppbv and 55.6±13.4 ppbv respectively (Event-II).  
446 Increased ozone concentrations during the high peak events have been analyzed using the  
447 satellite NO<sub>2</sub> concentration over the region considering the role of NO<sub>2</sub> as precursor for ozone  
448 formation. Daily total column NO<sub>2</sub> were obtained from OMI satellite (data available at the  
449 Giovanni platform; <http://giovanni.gsfc.nasa.gov/giovanni/>) at the spatial resolution of  
450 0.25°×0.25°. Figure 11 shows the NO<sub>2</sub> column value before, during and after both events. Even  
451 for the NO<sub>2</sub>, maximum concentrations were observed during these two special events.

### 452 3.3.2 Identifying regional contribution

453 An attempt has been undertaken to identify the source region contribution, utilizing the WRF-  
454 STEM model results, for the CO concentrations observed at Lumbini. A recent study (Kulkarni  
455 et al., 2015) has explored the source region contribution of various pollutants over the Central  
456 Asia using the same model. Figure 12 (A) shows the average contribution from different regions  
457 on CO concentration over Lumbini during the whole measurement period. Major share of CO  
458 was from the Ganges valley (46%) followed by Nepal region (25%) and rest of Indian region  
459 (~17.5%). Contribution from other South Asian countries like Bangladesh and Pakistan were ~  
460 11% whereas China contributed for ~1% of the CO concentration in Lumbini.

461 Figure 12 (B) is the time series of percentage contribution to total CO concentration during  
462 whole measurement period showing different air mass arriving at a 3 hourly intervals. During the  
463 whole measurement period, majority of the CO reaching Lumbini were from the Ganges valley



464 region with the contribution sometimes reaching up to ~80%. Other India (central, south, east  
465 and north) regions also contributed significantly. Bangladesh's contribution in CO loading was  
466 seen only after mid-April lasting for only about a week and after the first week of May. The  
467 contribution from Bangladesh was sporadic comparing to other regions. Highest contribution  
468 from this Bangladesh region was observed after the first week of June. Pakistan also contributed  
469 for the CO loading significantly. Others region as mentioned in the figure covered the regions  
470 like Afghanistan, Middle east, West Asia, East Asia, Africa and Bhutan. Contributions from  
471 these regions were less than 5%. Contribution from China was not evident till the first week of  
472 June where a specific air mass arrival shows contribution reaching up to 25% of total CO  
473 loading.

474 A sensitivity analysis was performed for emission uncertainty in the model grid containing  
475 Lumbini. Lumbini and surrounding regions in the recent years has seen significant rise in urban  
476 activities and industrial activity and related emissions which may not be accurately reflected in  
477 the HTAPv2 emissions inventory. A month long simulation was carried out with emissions from  
478 Lumbini and the surrounding four grids off and another simulation with Lumbini and  
479 surrounding four grid's emissions scaled 5 times the amount from HTAPv2 emissions inventory.  
480 The results are shown in Figure 12 (C) as percentage increase or decrease compared to model  
481 results using the current HTAPv2 emissions inventory. The black line shows concentration as  
482 100% for the current HTAPv2 emissions inventory. Despite making Lumbini and the  
483 surrounding grids emissions zero, model calculation shows pollutant concentration on average is  
484 still about 78% of the original value indicating dominance of background and regional sources  
485 compared to local source in the model. Increasing emissions 5 times for the Lumbini and  
486 surrounding four grids only increases the concentration on average by 151%. Thus uncertainty in  
487 emissions are not a local uncertainty for Lumbini rather for the whole region which needs to be  
488 better understood for improving model performance against observations at Lumbini.

### 489 **3.4 Contribution of aerosol composition to local air quality as identified by the model**

490 The chemical composition of  $PM_{2.5}$  obtained from the model is shown in Figure 13.  
491 Carbonaceous aerosols and sulfate pollutants contributed two-third fraction of the fine mode  
492 particulate matter ( $PM_{2.5}$ ). Organic carbon (OC) was found as the main constituent of the  $PM_{2.5}$



493 contributing ~ 45% to  $PM_{2.5}$ . For Lumbini, the contribution of modeled BC to  $PM_{2.5}$  was ~ 10%  
494 similar to the observed (9.2%) fraction of BC to  $PM_{2.5}$ . Recent study conducted over nearby IGP  
495 site, Kanpur (Ram and Sarin, 2011) found the average share of OC and EC in  $PM_{2.5}$  to be ~45%  
496 and ~5% respectively which is close to the values obtained by our model based calculation.  
497 Natural aerosols mainly wind-blown mineral dust was ~ 25% of the fine mode PM in Lumbini.  
498 Highest loading of dust is observed during the late dry period to early monsoon season in South  
499 Asian region (Adhikary et al., 2007). Sulfate contributed for ~ 20% share of the  $PM_{2.5}$  over  
500 Lumbini. Although the post monsoon season observed highest concentration of sulfate in South  
501 Asian region, elevated concentration are observed even during the April over Ganges Valley  
502 (Adhikary et al., 2007). As expected, very minimal contribution from sea salts (less than 1%)  
503 was observed at Lumbini.

### 504 **3.5 Does fossil fuel or biomass influence the Lumbini air?**

505 The aerosol spectral absorption is used to gain insight into nature and potential source of black  
506 carbon. This method enables to analyze the contributions of fossil fuel combustion and biomass  
507 burning contributions to the observed BC concentration (Kirchstetter et al., 2004). Besides BC,  
508 other light absorbing (in the UV region) aerosols are also produced in course of combustion,  
509 collectively termed as organic aerosols (often also called brown carbon or BrC) (Andreae and  
510 Gelencsér, 2006). Figure 14 shows the comparison of normalized light absorption as function of  
511 the wavelength for BC observed at Lumbini during cooking and non-cooking hours. Our results  
512 are compared with the published data of Kirchstetter et al. (2004) and that observed over a  
513 village center site of Project Surya in the IGP (Praveen et al., 2012) (figure not shown). We  
514 discuss light absorption data from two distinct times of the day. The main reason behind using  
515 data during 07:00-08:00 h and 16:00-17:00 h is these periods represent highest and lowest  
516 ambient concentration (Fig. 7). Also these period represent cooking and non-cooking or high and  
517 low vehicular movement hours (Praveen et al., 2012). To understand the influence of biomass  
518 and fossil fuel we plotted normalized aerosol absorption at 700 nm wavelength for complete  
519 aethalometer measured wavelengths in Fig. 14. Kirchstetter et al. (2004) reported OC absorption  
520 efficiency at 700 nm to be zero. Thus we normalized measured absorption spectrum by 700 nm  
521 wavelength absorption. Since aethalometer does not provide 700 nm wavelength absorption  
522 values, we used methodology followed by Praveen et al. (2012). Our results show that the



523 normalized absorption for biomass burning aerosol is ~3 times higher at 370 nm compared to  
524 that at 700 nm whereas fossil fuel absorption is about 2.6 times higher at the same wavelength.  
525 The normalized curve obtained during both cooking and non-cooking period lies in between the  
526 standard curve of Kirchstetter et al. (2004). The curve during the prime cooking time is much  
527 close to the biomass curve of published data (including that during the cooking period over the  
528 village center site of Project Surya) whereas that during non-cooking time (afternoon period) is  
529 inclined towards the fossil fuel curve. Similar result was also observed over the Project Surya  
530 village in the IGP region (Praveen et al., 2012; Rehman et al., 2011). This clearly indicates there  
531 is contribution of both sources: biomass as well as fossil fuel on the observed BC concentration  
532 over Lumbini.

533 In order to identify fractional contribution of biomass burning and fossil fuel combustion to  
534 observed BC aerosol, we adopted the method described by Sandradewi et al. (2008). Wavelength  
535 dependence of aerosol absorption coefficient ( $b_{\text{abs}}$ ) is proportional to  $\lambda^{-\alpha}$  where  $\lambda$  is the  
536 wavelength and  $\alpha$  is the absorption Ångstrom exponent. The  $\alpha$  values ranges from 0.9-2.2 for  
537 fresh wood smoke aerosol (Day et al., 2006) and between 0.8-1.1 for traffic or diesel soot  
538 (references in Sandradewi et al. (2008)). We have taken  $\alpha$  value of 1.86 for biomass burning and  
539 1.1 for fossil fuel burning as suggested by previous literature (Sandradewi et al., 2008). Figure  
540 15 shows diurnal variation of the biomass burning BC. Minimum contribution of biomass  
541 burning to total BC concentration was observed during 04:00-06:00 local time (only about 30%  
542 of the total BC). As the cooking activities start in morning, the contribution of biomass BC starts  
543 to increase and reaches about 50%. Similar pattern was repeated during evening cooking hours.  
544 Only during these two cooking periods, fossil fuel fraction BC was lower. Otherwise it remained  
545 significantly higher than biomass burning BC throughout the day. On average, ~40% of BC was  
546 from biomass burning whereas remaining 60% was contributed by fossil fuel combustion during  
547 our measurement period. Interestingly, this is the opposite of the contributions that were  
548 concluded by Lawrence and Lelieveld (2010). Lawrence and Lelieveld (2010) concluded that  
549 ~60% BC from biomass versus ~40% fossil fuel, based on a review of numerous previous  
550 studies to be likely for the outflow from Southern Asia during the winter monsoon. When we  
551 compared observed Ångstrom exponent with Praveen et al. (2012), we noticed that Lumbini  
552 values were lower than Project Surya Village center site. This implies Surya village center had



553 higher biomass fraction, also it was observed absorption Ångstrom exponent exceeded 1.86  
554 during cooking hours which indicates 100% biomass contribution. The difference is attributed to  
555 the fact that Lumbini sampling site is not a residential site like Surya village which can capture  
556 cooking influence efficiently. Further Lumbini sampling site is surrounded by commercial  
557 activities such as a local bus park, hotels, office buildings and industries and brick kilns slightly  
558 further away. Although the reason for this difference is not clear, it is an indication of the  
559 important role of diesel and coal emissions in the Lumbini and upwind regions.

#### 560 4 Conclusions

561 Our measurements, a first for the Lumbini area, have shown very high pollution concentration at  
562 Lumbini. Black carbon (BC), carbon monoxide (CO), ozone (O<sub>3</sub>) and particulate matter (PM<sub>10</sub>,  
563 PM<sub>2.5</sub> and PM<sub>1</sub>) were measured during the pre-monsoon of 2013 as a regional site of the *SusKat-*  
564 *ABC campaign*. Average pollutant concentrations during the monitoring period were found to be:  
565 BC:  $4.9 \pm 3.8 \mu\text{g m}^{-3}$ ; CO:  $344.1 \pm 160.3 \text{ ppbv}$ ; O<sub>3</sub>:  $46.6 \pm 20.3 \text{ ppbv}$ ; PM<sub>10</sub>:  $128.8 \pm 91.9 \mu\text{g m}^{-3}$  and  
566 PM<sub>2.5</sub>:  $53.14 \pm 35.1 \mu\text{g m}^{-3}$  which is comparable with other urban sites like Kanpur and Delhi. The  
567 diurnal variation of the pollutants is similar to that of any urban location, with peaks during  
568 morning and evening. However, our results show higher evening concentration compared to  
569 morning concentration values. During our measurement period, air quality in Lumbini was  
570 influenced by regional forest fires as shown by model and satellite data analysis. A regional  
571 chemical transport model, WRF-STEM was used to interpret observations. Inter-comparison of  
572 WRF-STEM model outputs with observations showed that the model underestimated the  
573 observed pollutant concentrations by a factor of 1.5 to 5. Nonetheless, WRF-STEM model was  
574 able to simulate the synoptic variability of observed pollutants. Model uncertainties are attributed  
575 mostly to uncertainties in meteorology and regional emissions. Region-tagged CO as air-mass  
576 tracers are employed in STEM to understand the source region influencing Lumbini. Our  
577 analysis shows that the adjacent regions; mostly the Ganges valley, other parts of India and  
578 Nepal accounted for the highest contribution to pollutant concentration in the Lumbini.  
579 Anthropogenic pollutants in PM<sub>2.5</sub> were dominant, with OC and BC contributing ~ 45% and  
580 ~10%, respectively while sulfate aerosol contributed to 20%, whereas natural pollutants like  
581 mineral dust contributed ~ 25%. The normalized light absorption curve clearly indicated the



582 contribution to BC in Lumbini from both sources: biomass as well as fossil fuel. On average,  
583 ~40% BC was found to be from the biomass burning and ~60% from fossil fuel burning.

584 Various improvements and extensions would be possible in future studies. More reliable  
585 functioning of the AWS (temperature and RH sensor, rain gauge) would have allowed more in-  
586 depth analysis of the relationship between meteorological parameters and pollutants  
587 concentration. Continuous measurements of air pollutants throughout the year would allow for  
588 annual and seasonal variation study. Improvements in the model are much needed in its ability to  
589 simulate observed meteorology. Significant uncertainty lies with regional emissions inventory  
590 and emissions from open burning.

591 There is a clear need for setting up of a continuous air quality monitoring station at Lumbini  
592 (UNESCO World Heritage Site) and the surrounding regions for long-term air quality  
593 monitoring. In order to fully safeguard the valuable world heritage properties as well as public  
594 health and agro-ecosystems in the region from impacts of air pollution, development activities  
595 within the Kenzo Tange Master Plan Area and Lumbini Protected Zone (LPZ) need to go  
596 through a rigorous environmental impact assessment (EIA) and heritage impact assessment  
597 (HIA) in accordance with the decisions of the UNESCO World Heritage Committee.

598

#### 599 **Data availability**

600 The data used for this manuscript can be obtained by sending an email to the corresponding  
601 authors and/or to IASS (Maheswar.Rupakheti@iass.potsdam.de) and/or to ICIMOD  
602 (arnico.panday@icimod.org). Modeling code can be obtained from B. Adhikary  
603 (Bhupesh.adhikary@icimod.org).

604

#### 605 **Authors' contributions**

606 M.R. designed the experiment. D.R. and K.S.M conducted the field observations. B.A. ran the  
607 WRF-STEM model. D.R., B.A., P.S.P., M.R. and S.K. conducted the data analysis, and D.R.  
608 prepared the manuscript with inputs from all coauthors.

609

610

611



## 612 Acknowledgements

613 This study was partly supported by the Institute for Advanced Sustainability Studies (IASS),  
614 Germany, the International Centre for Integrated Mountain Development (ICIMOD), and the  
615 National Natural Science Foundation of China (41121001, 41225002), and the Strategic Priority  
616 Research Program (B) of the Chinese Academy of Sciences (XDB03030504). D. Rupakheti  
617 would like to acknowledge the CAS-TWAS President PhD Fellowship program. ICIMOD  
618 authors would like to acknowledge that this study was partially supported by core funds of  
619 ICIMOD contributed by the governments of Afghanistan, Australia, Austria, Bangladesh,  
620 Bhutan, China, India, Myanmar, Nepal, Norway, Pakistan, Switzerland, and the United  
621 Kingdom. The views and interpretations in this publication are those of the authors and are not  
622 necessarily attributable to the institutions they are associated with. We thank B. Kathayat, B.R.  
623 Bhatta, and Venerable Vivekananda and his colleagues (Panditarama Lumbini International  
624 Vipassana Meditation Center) for providing logistical support which was vital in setting up and  
625 running the site. We also thank C. Cüppers and M. Pahlke of the Lumbini International Research  
626 Institute (LIRI) for providing the space and power to run the instruments at the LIRI premises.  
627 Satellite data providers (MODIS, AIRS, OMI) are also equally acknowledged.

628

629



## 630 References

- 631 Adhikary, B., Carmichael, G. R., Tang, Y., Leung, L. R., Qian, Y., Schauer, J. J., Stone, E. A.,  
632 Ramanathan, V., and Ramana, M. V.: Characterization of the seasonal cycle of south Asian aerosols: A  
633 regional-scale modeling analysis, *J. Geophys. Res.*, 112, D22S22, doi: 10.1029/2006jd008143, 2007.
- 634 Andreae, M. O., and Gelencsér, A.: Black carbon or brown carbon? The nature of light-absorbing  
635 carbonaceous aerosols, *Atmos. Chem. Phys.*, 6, 3131-3148, doi: 10.5194/acp-6-3131-2006, 2006.
- 636 Badarinath, K., Sharma, A. R., Kharol, S. K., and Prasad, V. K.: Variations in CO, O<sub>3</sub> and black carbon  
637 aerosol mass concentrations associated with planetary boundary layer (PBL) over tropical urban  
638 environment in India, *J. Atmos. Chem.*, 62, 73-86, doi: 10.1007/s10874-009-9137-2, 2009.
- 639 Baedecker, P. A., Reddy, M. M., Reimann, K. J., and Sciammarella, C. A.: Effects of acidic deposition on  
640 the erosion of carbonate stone — experimental results from the U.S. National Acid Precipitation  
641 Assessment Program (NAPAP), *Atmos. Environ.*, 26, 147-158, doi: 10.1016/0957-1272(92)90018-N,  
642 1992.
- 643 Bergin, M. H., Tripathi, S. N., Jai Devi, J., Gupta, T., McKenzie, M., Rana, K., Shafer, M. M., Villalobos,  
644 A. M., and Schauer, J. J.: The Discoloration of the Taj Mahal due to Particulate Carbon and Dust  
645 Deposition, *Environ. Sci. Technol.*, 49, 808-812, doi: 10.1021/es504005q, 2015.
- 646 Bisht, D. S., Dumka, U. C., Kaskaoutis, D. G., Pipal, A. S., Srivastava, A. K., Soni, V. K., Attri, S. D.,  
647 Sateesh, M., and Tiwari, S.: Carbonaceous aerosols and pollutants over Delhi urban environment:  
648 Temporal evolution, source apportionment and radiative forcing, *Sci. Total Environ.*, 521-522C, 431-445,  
649 doi: 10.1016/j.scitotenv.2015.03.083, 2015.
- 650 Bonasoni, P., Laj, P., Marinoni, A., Sprenger, M., Angelini, F., Arduini, J., Bonafè, U., Calzolari, F.,  
651 Colombo, T., Decesari, S., Di Biagio, C., di Sarra, A. G., Evangelisti, F., Duchi, R., Facchini, M. C.,  
652 Fuzzi, S., Gobbi, G. P., Maione, M., Panday, A., Roccatò, F., Sellegri, K., Venzac, H., Verza, G. P.,  
653 Villani, P., Vuillermoz, E., and Cristofanelli, P.: Atmospheric Brown Clouds in the Himalayas: first two  
654 years of continuous observations at the Nepal Climate Observatory-Pyramid (5079 m), *Atmos. Chem.*  
655 *Phys.*, 10, 7515-7531, doi: 10.5194/acp-10-7515-2010, 2010.
- 656 Brimblecombe, P.: The effects of air pollution on the built environment, Imperial College Press, London,  
657 2003.
- 658 Burney, J., and Ramanathan, V.: Recent climate and air pollution impacts on Indian agriculture, *Proc.*  
659 *Natl. Acad. Sci. USA*, 111, 16319-16324, doi: 10.1073/pnas.1317275111, 2014.
- 660 Cong, Z., Kang, S., Kawamura, K., Liu, B., Wan, X., Wang, Z., Gao, S., and Fu, P.: Carbonaceous  
661 aerosols on the south edge of the Tibetan Plateau: concentrations, seasonality and sources, *Atmos. Chem.*  
662 *Phys.*, 15, 1573-1584, doi: 10.5194/acp-15-1573-2015, 2015a.
- 663 Cong, Z., Kawamura, K., Kang, S., and Fu, P.: Penetration of biomass-burning emissions from South  
664 Asia through the Himalayas: new insights from atmospheric organic acids, *Sci. Rep.*, 5, doi:  
665 10.1038/srep09580, 2015b.
- 666 Cristofanelli, P., Bracci, A., Sprenger, M., Marinoni, A., Bonafè, U., Calzolari, F., Duchi, R., Laj, P.,  
667 Pichon, J. M., Roccatò, F., Venzac, H., Vuillermoz, E., and Bonasoni, P.: Tropospheric ozone variations



- 668 at the Nepal Climate Observatory-Pyramid (Himalayas, 5079 m a.s.l.) and influence of deep stratospheric  
669 intrusion events, *Atmos. Chem. Phys.*, 10, 6537-6549, doi: 10.5194/acp-10-6537-2010, 2010.
- 670 Das, S. K., and Jayaraman, A.: Role of black carbon in aerosol properties and radiative forcing over  
671 western India during premonsoon period, *Atmos. Res.*, 102, 320-334, doi:  
672 10.1016/j.atmosres.2011.08.003, 2011.
- 673 Day, D., Hand, J., Carrico, C., Engling, G., and Malm, W.: Humidification factors from laboratory studies  
674 of fresh smoke from biomass fuels, *J. Geophys. Res.*, 111, D22202, doi: 10.1029/2006JD007221, 2006.
- 675 Duchi, R., Cristofanelli, P., Marinoni, A., Laj, P., Marcq, S., Villani, P., Sellegri, K., Angelini, F.,  
676 Calzolari, F., Gobbi, G. P., Verza, G. P., Vuillermoz, E., Sapkota, A., and Bonasoni, P.: Continuous  
677 observations of synoptic-scale dust transport at the Nepal Climate Observatory-Pyramid (5079 m a.s.l.) in  
678 the Himalayas, *Atmos. Chem. Phys. Discuss.*, 11, 4229-4261, doi: 10.5194/acpd-11-4229-2011, 2011.
- 679 Forouzanfar, M. H., Alexander, L., Anderson, H. R., Bachman, V. F., Biryukov, S., Brauer, M., Burnett,  
680 R., Casey, D., Coates, M. M., and Cohen, A.: Global, regional, and national comparative risk assessment  
681 of 79 behavioural, environmental and occupational, and metabolic risks or clusters of risks in 188  
682 countries, 1990–2013: a systematic analysis for the Global Burden of Disease Study 2013, *Lancet*, 386,  
683 2287-2323, doi: 10.1016/S0140-6736(15)00128-2, 2015.
- 684 Ganguly, D., Jayaraman, A., Rajesh, T. A., and Gadhavi, H.: Wintertime aerosol properties during foggy  
685 and nonfoggy days over urban center Delhi and their implications for shortwave radiative forcing, *J.*  
686 *Geophys. Res.*, 111, D15217, doi: 10.1029/2005jd007029, 2006.
- 687 Gaur, A., Tripathi, S. N., Kanawade, V. P., Tare, V., and Shukla, S. P.: Four-year measurements of trace  
688 gases (SO<sub>2</sub>, NO<sub>x</sub>, CO, and O<sub>3</sub>) at an urban location, Kanpur, in Northern India, *J. Atmos. Chem.*, 71,  
689 283-301, doi: 10.1007/s10874-014-9295-8, 2014.
- 690 Gauri, K. L., and Holdren, G.: Pollutant effects on stone monuments, *Environ. Sci. Technol.*, 15, 386-390,  
691 doi: 10.1021/es00086a001, 1981.
- 692 Hegde, P., Pant, P., and Bhavani Kumar, Y.: An integrated analysis of lidar observations in association  
693 with optical properties of aerosols from a high altitude location in central Himalayas, *Atmos. Sci. Lett.*,  
694 10, 48-57, doi: 10.1002/asl.209, 2009.
- 695 IPCC: Climate Change 2013: The Physical Science Basis. Contribution of Working Group I to the Fifth  
696 Assessment Report of the Intergovernmental Panel on Climate Change [Stocker, T.F., D. Qin, G.-K.  
697 Plattner, M. Tignor, S.K. Allen, J. Boschung, A. Nauels, Y. Xia, V. Bex and P.M. Midgley (eds.)], 2013.
- 698 Joshi, H., Naja, M., Singh, K., Kumar, R., Bhardwaj, P., Babu, S. S., Satheesh, S., Moorthy, K. K., and  
699 Chandola, H.: Investigations of aerosol black carbon from a semi-urban site in the Indo-Gangetic Plain  
700 region, *Atmos. Environ.*, 125, 346-359, doi: 10.1016/j.atmosenv.2015.04.007, 2016.
- 701 Kirchstetter, T. W., Novakov, T., and Hobbs, P. V.: Evidence that the spectral dependence of light  
702 absorption by aerosols is affected by organic carbon, *J. Geophys. Res.*, 109, D21208,  
703 doi:10.1029/2004JD004999, 2004.
- 704 Kulkarni, S., Sobhani, N., Miller-Schulze, J. P., Shafer, M. M., Schauer, J. J., Solomon, P. A., Saide, P.  
705 E., Spak, S. N., Cheng, Y. F., Denier van der Gon, H. A. C., Lu, Z., Streets, D. G., Janssens-Maenhout,



- 706 G., Wiedinmyer, C., Lantz, J., Artamonova, M., Chen, B., Imashev, S., Sverdlik, L., Deminter, J. T.,  
707 Adhikary, B., D'Allura, A., Wei, C., and Carmichael, G. R.: Source sector and region contributions to BC  
708 and PM<sub>2.5</sub> in Central Asia, *Atmos. Chem. Phys.*, 15, 1683-1705, doi: 10.5194/acp-15-1683-2015, 2015.
- 709 Kumar, V., Sarkar, C., and Sinha, V.: Influence of post harvest crop residue fires on surface ozone mixing  
710 ratios in the NW IGP analyzed using two years of continuous in-situ trace gas measurements, *J. Geophys.*  
711 *Res. Atmos.*, 121, 3619–3633, doi: 10.1002/2015JD024308, 2016.
- 712 Lawrence, M. G., and Lelieveld, J.: Atmospheric pollutant outflow from southern Asia: a review, *Atmos.*  
713 *Chem. Phys.*, 10, 11017-11096, doi: 10.5194/acp-10-11017-2010, 2010.
- 714 Lüthi, Z. L., Škerlak, B., Kim, S. W., Lauer, A., Mues, A., Rupakheti, M., and Kang, S.: Atmospheric  
715 brown clouds reach the Tibetan Plateau by crossing the Himalayas, *Atmos. Chem. Phys.*, 15, 6007-6021,  
716 doi: 10.5194/acp-15-6007-2015, 2015.
- 717 Marinoni, A., Cristofanelli, P., Laj, P., Duchi, R., Putero, D., Calzolari, F., Landi, T. C., Vuillermoz, E.,  
718 Maione, M., and Bonasoni, P.: High black carbon and ozone concentrations during pollution transport in  
719 the Himalayas: Five years of continuous observations at NCO-P global GAW station, *J. Environ. Sci.-*  
720 *China*, 25, 1618-1625, doi: 10.1016/s1001-0742(12)60242-3, 2013.
- 721 Mohnen, V. A., Goldstein, W., and Wang, W. C.: Tropospheric Ozone and Climate Change, *Air & Waste*,  
722 43, 1332-1334, doi: 10.1080/1073161x.1993.10467207, 1993.
- 723 Naja, M., Lal, S., and Chand, D.: Diurnal and seasonal variabilities in surface ozone at a high altitude site  
724 Mt Abu (24.6° N, 72.7° E, 1680m asl) in India, *Atmos. Environ.*, 37, 4205-4215, doi: 10.1016/S1352-  
725 2310(03)00565-X, 2003.
- 726 Naja, M., Mallik, C., Sarangi, T., Sheel, V., and Lal, S.: SO<sub>2</sub> measurements at a high altitude site in the  
727 central Himalayas: Role of regional transport, *Atmos. Environ.*, 99, 392-402, doi:  
728 10.1016/j.atmosenv.2014.08.031, 2014.
- 729 Panday, A. K., and Prinn, R. G.: Diurnal cycle of air pollution in the Kathmandu Valley, Nepal:  
730 Observations, *J. Geophys. Res.*, 114, D09305, doi: 10.1029/2008jd009777, 2009.
- 731 Patil, M., Patil, S., Waghmare, R., and Dharmaraj, T.: Planetary Boundary Layer and aerosol interactions  
732 over the Indian sub-continent, *J. Atmos. Sol.-Terr. Phys.*, 112, 38-42, doi: 10.1016/j.jastp.2014.02.007,  
733 2014.
- 734 Praveen, P. S., Ahmed, T., Kar, A., Rehman, I. H., and Ramanathan, V.: Link between local scale BC  
735 emissions in the Indo-Gangetic Plains and large scale atmospheric solar absorption, *Atmos. Chem. Phys.*,  
736 12, 1173-1187, doi: 10.5194/acp-12-1173-2012, 2012.
- 737 Putero, D., Landi, T., Cristofanelli, P., Marinoni, A., Laj, P., Duchi, R., Calzolari, F., Verza, G., and  
738 Bonasoni, P.: Influence of open vegetation fires on black carbon and ozone variability in the southern  
739 Himalayas (NCO-P, 5079 m asl), *Environ. Pollut.*, 184, 597-604, doi: 10.1016/j.envpol.2013.09.035,  
740 2014.
- 741 Putero, D., Cristofanelli, P., Marinoni, A., Adhikary, B., Duchi, R., Shrestha, S. D., Verza, G. P., Landi,  
742 T. C., Calzolari, F., Busetto, M., Agrillo, G., Biancofiore, F., Di Carlo, P., Panday, A. K., Rupakheti, M.,  
743 and Bonasoni, P.: Seasonal variation of ozone and black carbon observed at Paknajol, an urban site in the



- 744 Kathmandu Valley, Nepal, Atmos. Chem. Phys. Discuss., 15, 22527-22566, 10.5194/acpd-15-22527-  
745 2015, 2015.
- 746 Ram, K., Sarin, M., and Tripathi, S.: A 1 year record of carbonaceous aerosols from an urban site in the  
747 Indo-Gangetic Plain: Characterization, sources, and temporal variability, J. Geophys. Res., 115, D24313,  
748 doi: 10.1029/2010JD014188, 2010.
- 749 Ram, K., and Sarin, M. M.: Day–night variability of EC, OC, WSOC and inorganic ions in urban  
750 environment of Indo-Gangetic Plain: Implications to secondary aerosol formation, Atmos. Environ., 45,  
751 460-468, doi: 10.1016/j.atmosenv.2010.09.055, 2011.
- 752 Ramanathan, V., Li, F., Ramana, M., Praveen, P., Kim, D., Corrigan, C., Nguyen, H., Stone, E. A.,  
753 Schauer, J. J., and Carmichael, G.: Atmospheric brown clouds: Hemispherical and regional variations in  
754 long-range transport, absorption, and radiative forcing, J. Geophys. Res., 112, D22S21, doi:  
755 10.1029/2006JD008124, 2007.
- 756 Ramanathan, V., and Carmichael, G.: Global and regional climate changes due to black carbon, Nat.  
757 Geosci., 1, 221-227, 2008.
- 758 Rastogi, N., Singh, A., Sarin, M. M., and Singh, D.: Temporal variability of primary and secondary  
759 aerosols over northern India: Impact of biomass burning emissions, Atmos. Environ., 125, 396-403, doi:  
760 10.1016/j.atmosenv.2015.06.010, 2016.
- 761 Rehman, I. H., Ahmed, T., Praveen, P. S., Kar, A., and Ramanathan, V.: Black carbon emissions from  
762 biomass and fossil fuels in rural India, Atmospheric Chemistry and Physics, 11, 7289-7299, 10.5194/acp-  
763 11-7289-2011, 2011.
- 764 Safai, P. D., Kewat, S., Pandithurai, G., Praveen, P. S., Ali, K., Tiwari, S., Rao, P. S. P., Budhawant, K.  
765 B., Saha, S. K., and Devara, P. C. S.: Aerosol characteristics during winter fog at Agra, North India, J.  
766 Atmos. Chem., 61, 101-118, doi: 10.1007/s10874-009-9127-4, 2009.
- 767 Sandradewi, J., Prévôt, A. S. H., Szidat, S., Perron, N., Alfarra, M. R., Lanz, V. A., Weingartner, E., and  
768 Baltensperger, U.: Using Aerosol Light Absorption Measurements for the Quantitative Determination of  
769 Wood Burning and Traffic Emission Contributions to Particulate Matter, Environ. Sci. Technol., 42,  
770 3316-3323, doi: 10.1021/es702253m, 2008.
- 771 Sarkar, C., Kumar, V., and Sinha, V.: Massive emissions of carcinogenic benzenoids from paddy residue  
772 burning in north India, Curr. Sci. India, 104, 1703-1709, 2013.
- 773 Schmid, O., Artaxo, P., Arnott, W. P., Chand, D., Gatti, L. V., Frank, G. P., Hoffer, A., Schnaiter, M., and  
774 Andreae, M. O.: Spectral light absorption by ambient aerosols influenced by biomass burning in the  
775 Amazon Basin. I: Comparison and field calibration of absorption measurement techniques, Atmos. Chem.  
776 Phys., 6, 3443-3462, doi: 10.5194/acp-6-3443-2006, 2006.
- 777 Sharma, R. K., Bhattarai, B. K., Sapkota, B. K., Gewali, M. B., and Kjeldstad, B.: Black carbon aerosols  
778 variation in Kathmandu valley, Nepal, Atmos. Environ., 63, 282-288, doi:  
779 10.1016/j.atmosenv.2012.09.023, 2012.
- 780 Shindell, D.: Integrated Assessment of Black Carbon and Tropospheric Ozone: Summary for Decision  
781 Makers, United Nations Environment Programme, 2011.



- 782 Sinha, V., Kumar, V., and Sarkar, C.: Chemical composition of pre-monsoon air in the Indo-Gangetic  
783 Plain measured using a new air quality facility and PTR-MS: high surface ozone and strong influence of  
784 biomass burning, *Atmos. Chem. Phys.*, 14, 5921-5941, doi: 10.5194/acp-14-5921-2014, 2014.
- 785 Skamarock, W., Klemp, J., Dudhia, J., Gill, D., and Barker, D.: A description of the Advanced Research  
786 WRF version 3, Technical Report NCAR/TN475+STR, National Center for Atmospheric Research  
787 Technical Note, Boulder, Colorado, 2008.
- 788 Srivastava, A. K., Tiwari, S., Devara, P. C. S., Bisht, D. S., Srivastava, M. K., Tripathi, S. N., Goloub, P.,  
789 and Holben, B. N.: Pre-monsoon aerosol characteristics over the Indo-Gangetic Basin: implications to  
790 climatic impact, *Ann. Geophys.*, 29, 789-804, doi: 10.5194/angeo-29-789-2011, 2011.
- 791 Stevenson, D., Dentener, F., Schultz, M., Ellingsen, K., Van Noije, T., Wild, O., Zeng, G., Amann, M.,  
792 Atherton, C., and Bell, N.: Multimodel ensemble simulations of present-day and near-future tropospheric  
793 ozone, *J. Geophys. Res.*, 111, D08301, doi: 10.1029/2005JD006338, 2006.
- 794 WHO: Air quality guidelines: global update 2005: particulate matter, ozone, nitrogen dioxide, and sulfur  
795 dioxide, World Health Organization, 2006.
- 796 Wiedinmyer, C., Akagi, S. K., Yokelson, R. J., Emmons, L. K., Al-Saadi, J. A., Orlando, J. J., and Soja,  
797 A. J.: The Fire INventory from NCAR (FINN): a high resolution global model to estimate the emissions  
798 from open burning, *Geosci. Model Dev.*, 4, 625-641, doi: 10.5194/gmd-4-625-2011, 2011.
- 799 Xu, B., Cao, J., Hansen, J., Yao, T., Joswita, D. R., Wang, N., Wu, G., Wang, M., Zhao, H., Yang, W.,  
800 Liu, X., and He, J.: Black soot and the survival of Tibetan glaciers, *Proc. Natl. Acad. Sci. USA*, 106,  
801 22114-22118, doi: 10.1073/pnas.0910444106, 2009.

802



803 **Table 1.** Summary of instruments deployed during monitoring in Lumbini

Instrument (Model)	Manufacturer	Parameters	Inlet/sensor height (above ground)	Sampling interval	Sampled period
Environmental Dust monitor (EDM 164)	GRIMM Aerosol Technik, Germany	PM <sub>10</sub> , PM <sub>2.5</sub> , PM <sub>1</sub>	5 m	5 min	01/04-15/06
Aethalometer (AE42)	Magee Scientific, USA	Aerosol light absorption at seven wavelengths, and BC concentration	3 m	5 min	01/04-05/06
CO analyzer (48i)	Thermo Scientific, USA	CO concentration	3 m	1 min	01/04-15/06
O <sub>3</sub> analyzer (49i)	Thermo Scientific, USA	O <sub>3</sub> concentration	3 m	1 min	01/04-15/06
Automatic Weather Station (AWS)	Campbell Scientific, UK	T, RH, WS, WD, Global Radiation, Precipitation	12 m	1 min	01/04-15/06

804

805

28



806 **Table 2.** Comparison of PM<sub>2.5</sub>, BC, CO and O<sub>3</sub> concentrations at Lumbini with those at other sites in South Asia

Sites	Characteristics	Measurement period	PM <sub>2.5</sub> (µg m <sup>-3</sup> )	BC (µg/m <sup>3</sup> )	CO (ppbv)	O <sub>3</sub> (ppbv)	References
Lumbini, Nepal	Semi-urban	Pre-monsoon, 2013	53.1±35.1	4.9±3.8	344.1±160.3	46.6±20.3	This study
Kathmandu, Nepal	Urban	Pre-monsoon, 2013	-	14.5±10	-	38.0±25.6	(Putero et al., 2015)
Mt. Everest, Nepal	Remote	Pre-monsoon	-	0.4±0.4	-	61.3±7.7	(Marinoni et al., 2013)
Delhi, India	Urban	Pre-monsoon (night-time)	82.3±50.5	7.70±7.25	1800±890	-	(Bisht et al., 2015)
Kanpur, India	Urban	June 2009-May 2013, April-June 2013	-	2.1±0.9	721±403	27.9±17.8	(Gaur et al., 2014) (Ram et al., 2010)
Mohali, India	Semi-urban	May, 2012	104±80.3	-	566.7±239.2	57.8±25.4	(Sinha et al., 2014)
Mt. Abu, India	Remote	Jan 1993-Dec 2000, pre-monsoon	-	0.7±0.14	131±36	39.9±10.8	(Naja et al., 2003) (Das and Jayaraman, 2011)

807

808

809



810 **Table 3.** Inter-comparison of observed and model simulated hourly average concentrations of air  
811 pollutants during the measurement campaign period. Unit: PM and BC in  $\mu\text{g}/\text{m}^3$  and CO in ppbv.

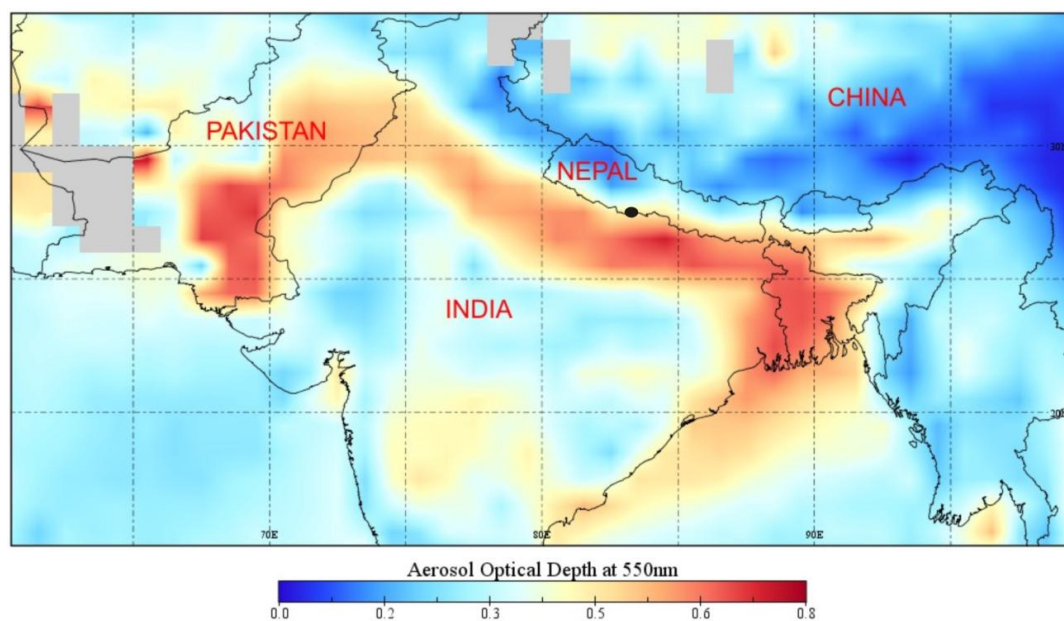
Pollutants	Observed (mean and range)	Modeled (mean and range)	Ratio of mean (observed/modeled)
PM <sub>10</sub>	128.8 (10.5-604.0)	25.4 (2.1-68.8)	5
PM <sub>2.5</sub>	53.1 (6.1-272.2)	17.3 (1.9-48.3)	3
CO	344.1(124.9-1429.7)	255.7 (72.2-613.1)	1.4
BC	4.9 (0.3-29.9)	1.8 (0.4-3.7)	2.7

812

813



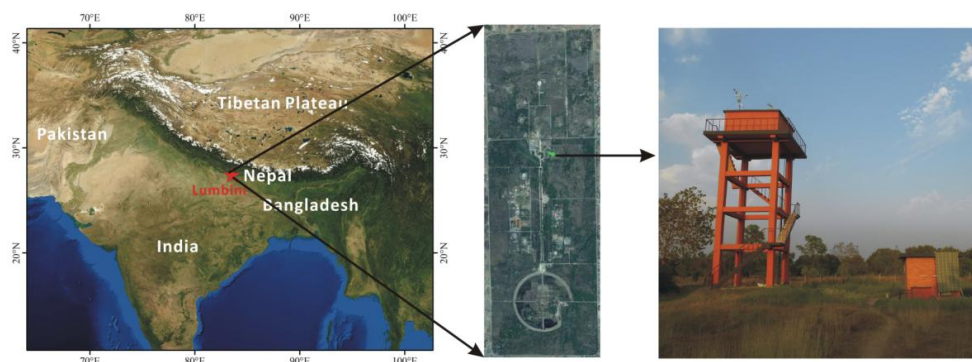
814 **Figures**



815

816 **Figure 1.** Aerosol optical depth in South Asia acquired with the MODIS instrument aboard  
817 TERRA satellite averaged over the winter and pre-monsoon season (December 2012-June 2013).  
818 High aerosol loading can be seen over the entire Indo-Gangetic Plains (IGP). An aerosol hotspot  
819 south of Lumbini (small black mark nearby the border of Nepal with India) is clearly visible.  
820 Light grey color used in the figure represents the absence of data.

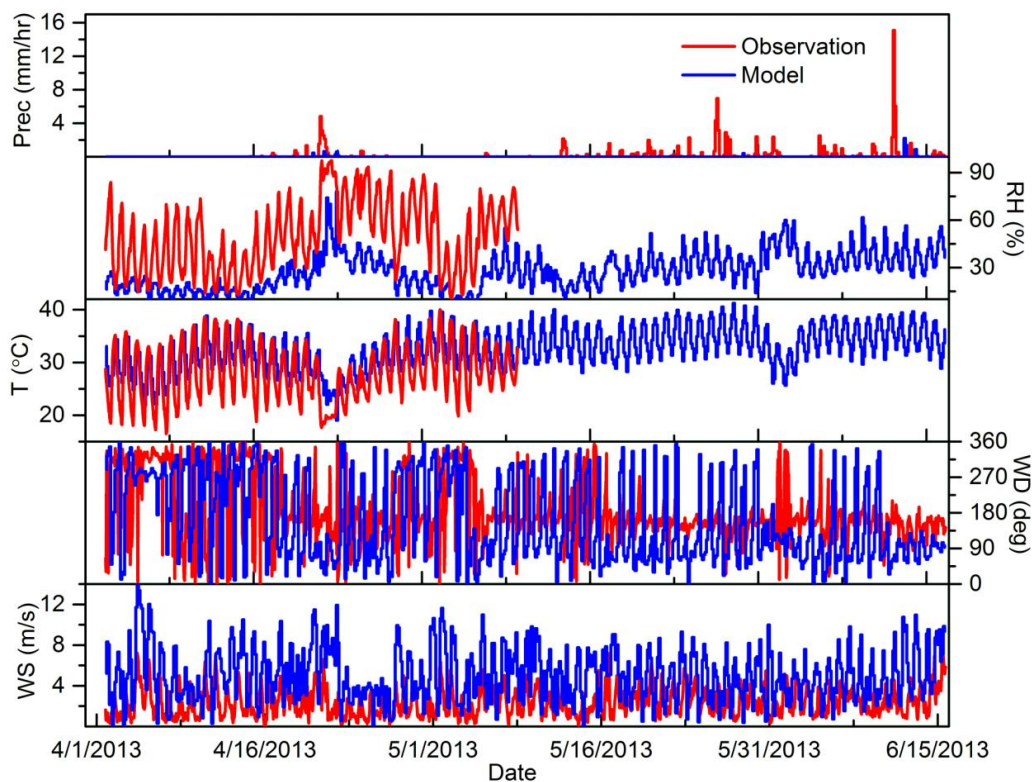
821



822

823 **Figure 2.** Location of sampling site in Lumbini in southern Nepal (left panel). The middle panel  
824 shows the Kenzo Tange Master Plan Area of Lumbini while the right panel shows the sampling  
825 tower in the Lumbini Master Plan Area.

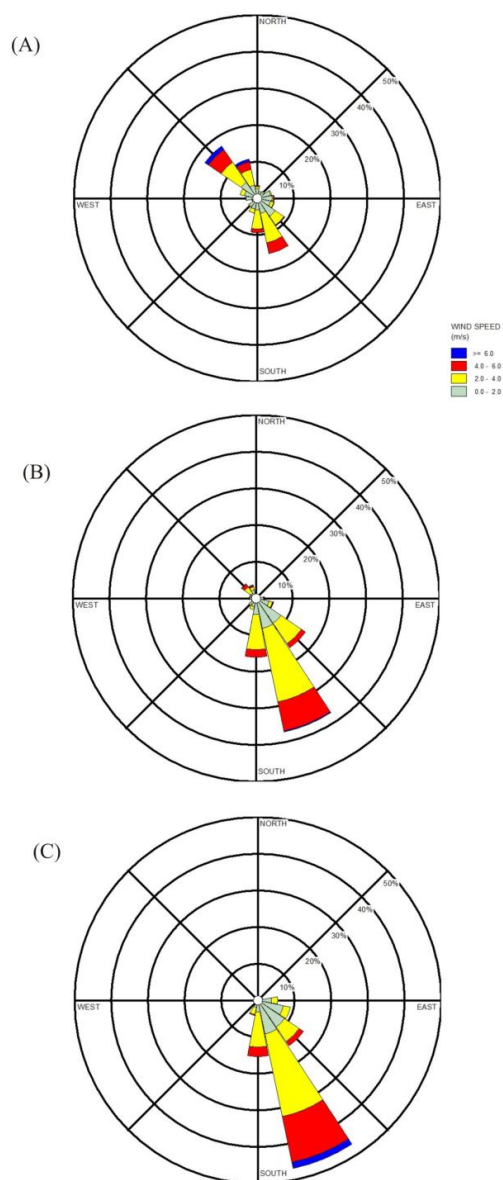
826



827

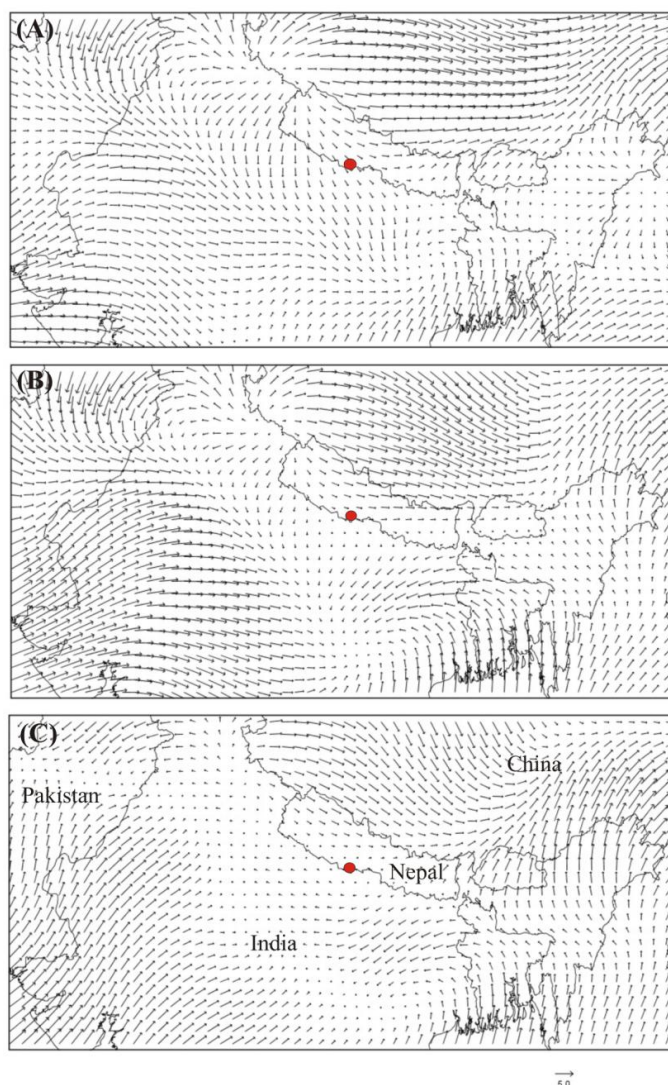
828 **Figure 3.** Time series of hourly average observed (red line) and model estimated (blue line)  
829 meteorological parameters at Lumbini, Nepal for the entire sampling period from 1 April to 15  
830 June 2013.

831



832

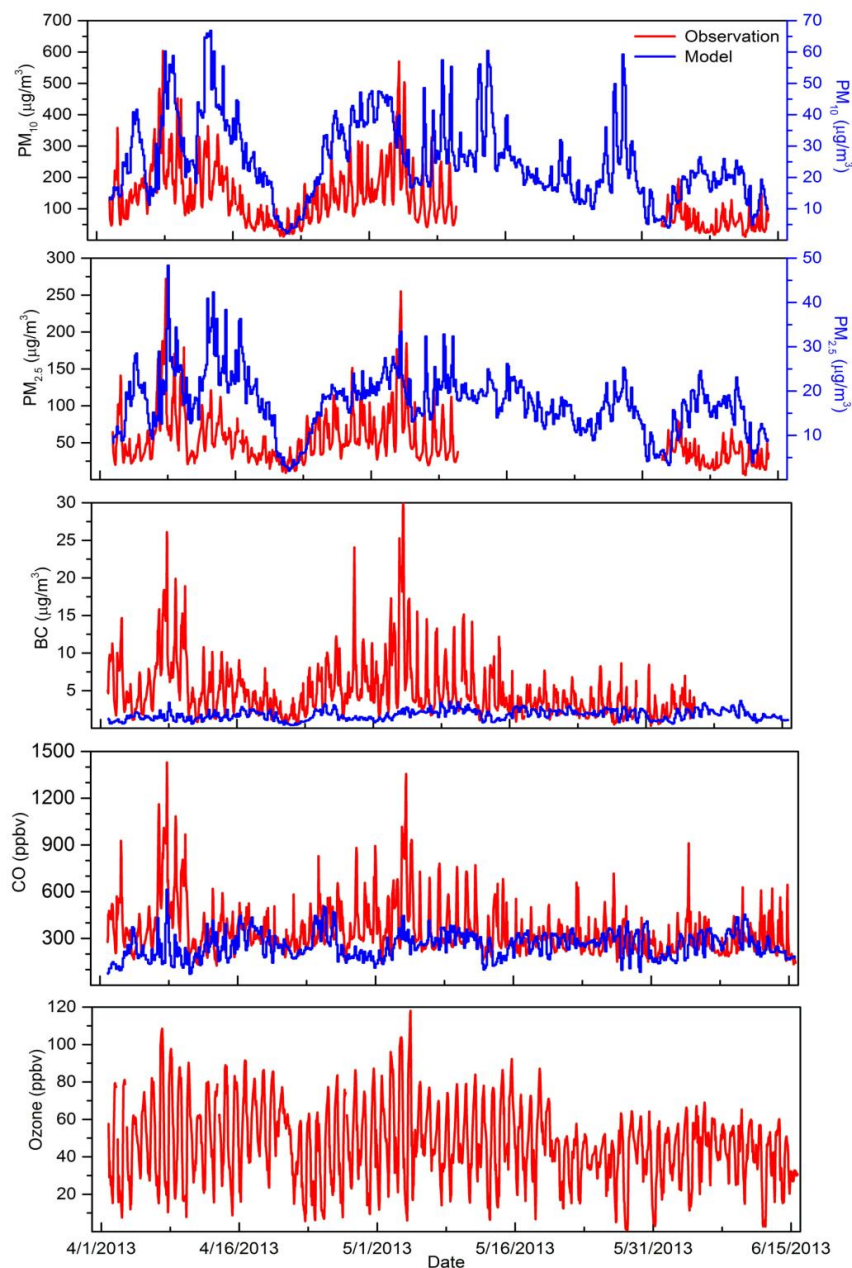
833 **Figure 4.** Wind rose of wind speed and wind direction observed at Lumbini during the month of  
834 (A) April, (B) May, and (C) (1<sup>st</sup>-15<sup>th</sup>) June 2013.



835

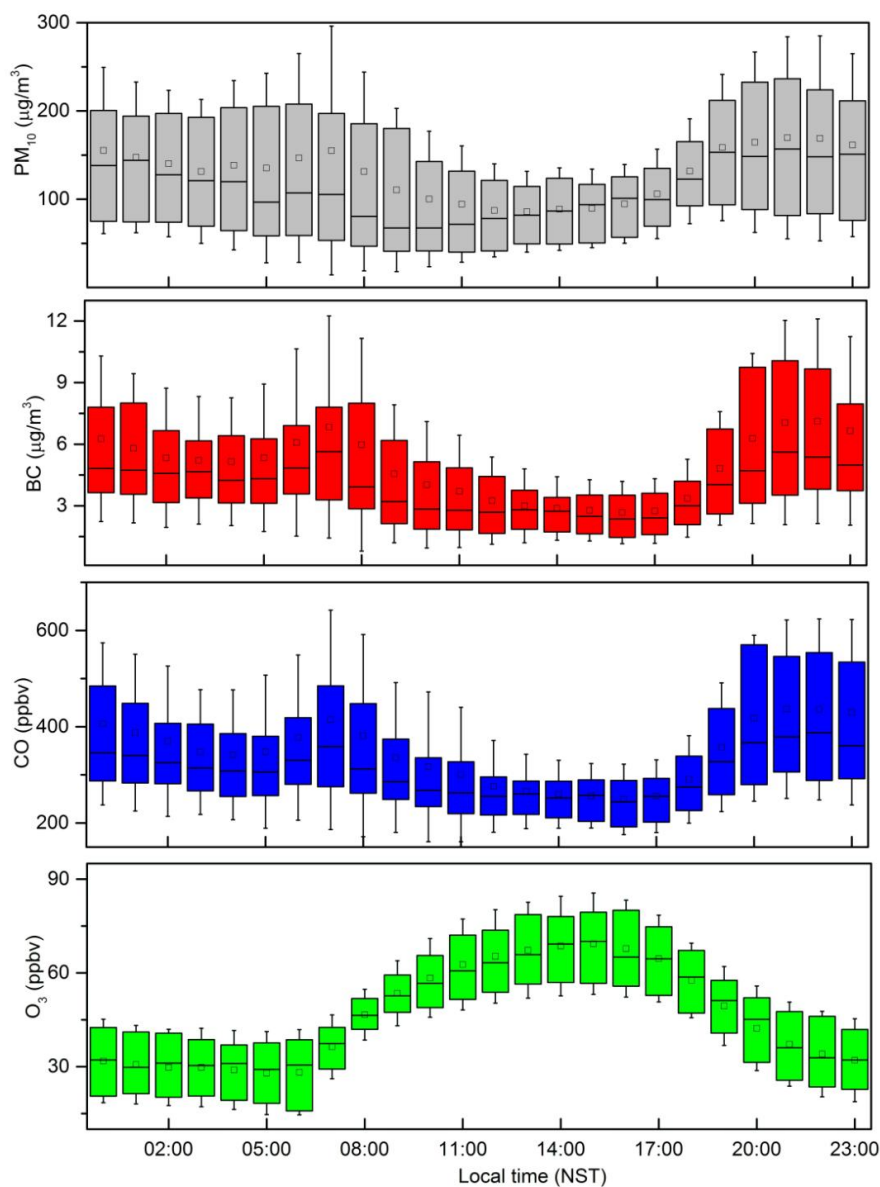
836 **Figure 5.** Monthly synoptic surface winds for the month of (A) April, (B) May and (C) June  
837 2013, based on NCEP/NCAR reanalysis data. Orientations of arrows in the figures refer to wind  
838 direction whereas the length of arrows represents the magnitude of wind speed (m/s). Red dot in  
839 the map represents the location of Lumbini.

840



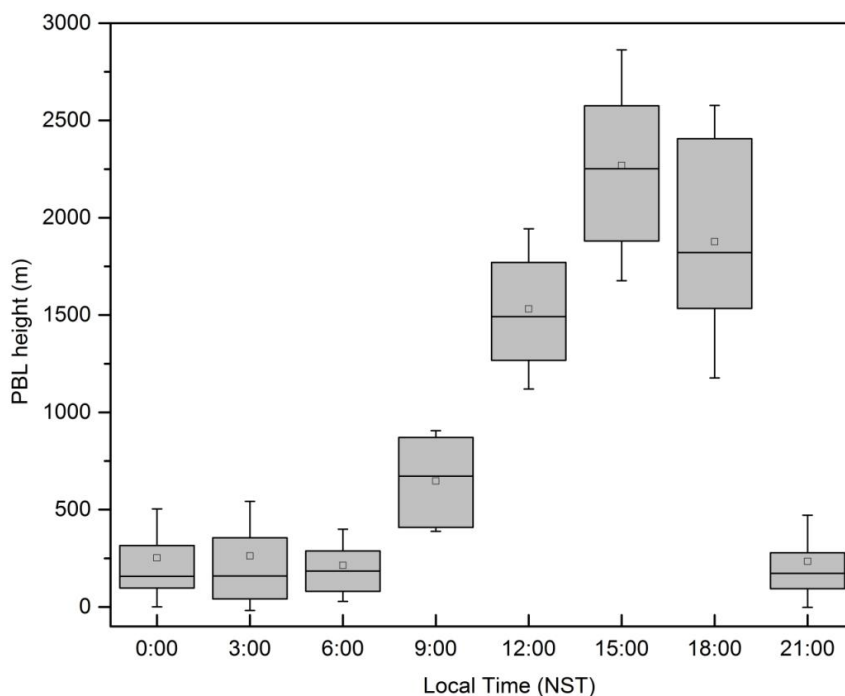
841

842 **Figure 6.** Time series of the observed (red line) and model estimated (blue line) hourly average  
843 concentrations of PM<sub>10</sub>, PM<sub>2.5</sub>, BC, CO and O<sub>3</sub> at Lumbini, Nepal for the entire sampling period  
844 from 1 April to 15 June 2013. Model estimated O<sub>3</sub> was not available.



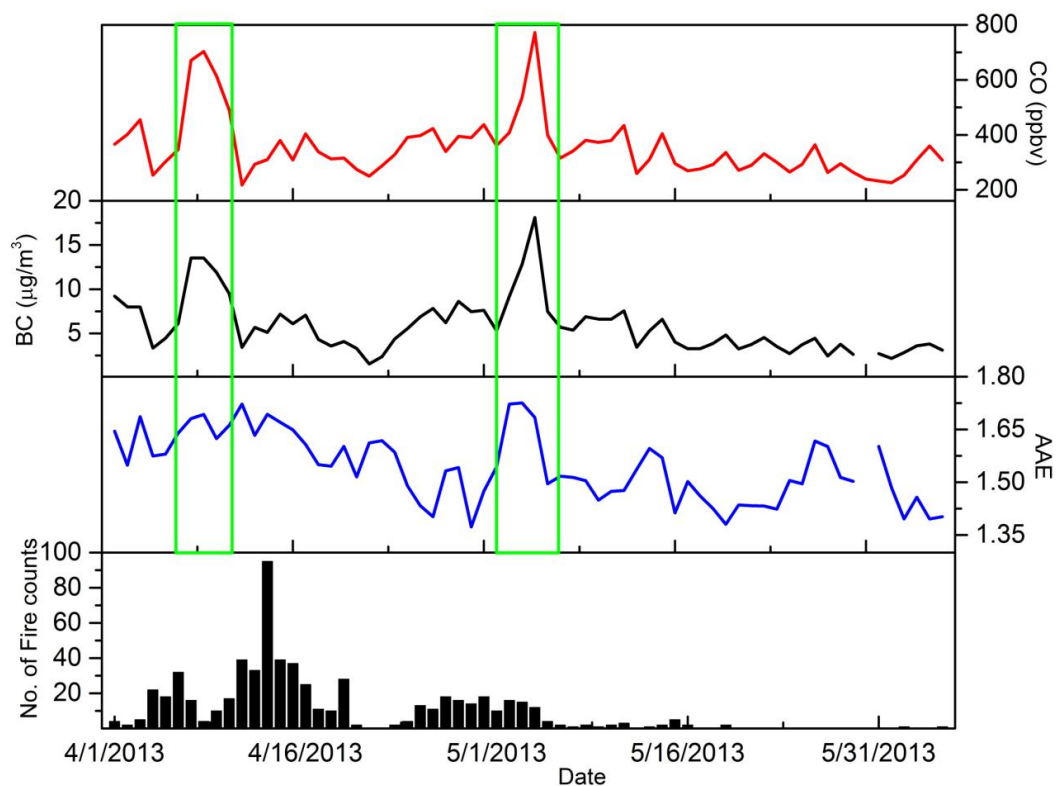
845

846 **Figure 7.** Diurnal variations of hourly average ambient concentrations of PM<sub>10</sub>, BC, CO and O<sub>3</sub>  
847 at Lumbini during the monitoring period (1 April -15 June 2013). In each box, lower and upper  
848 boundary of the box represents 25<sup>th</sup> and 75<sup>th</sup> percentile respectively, top and bottom of the  
849 whisker represents 90<sup>th</sup> and 10<sup>th</sup> percentile respectively, the mid-line represents median, and the  
850 square mark represents the mean for each hour.



851

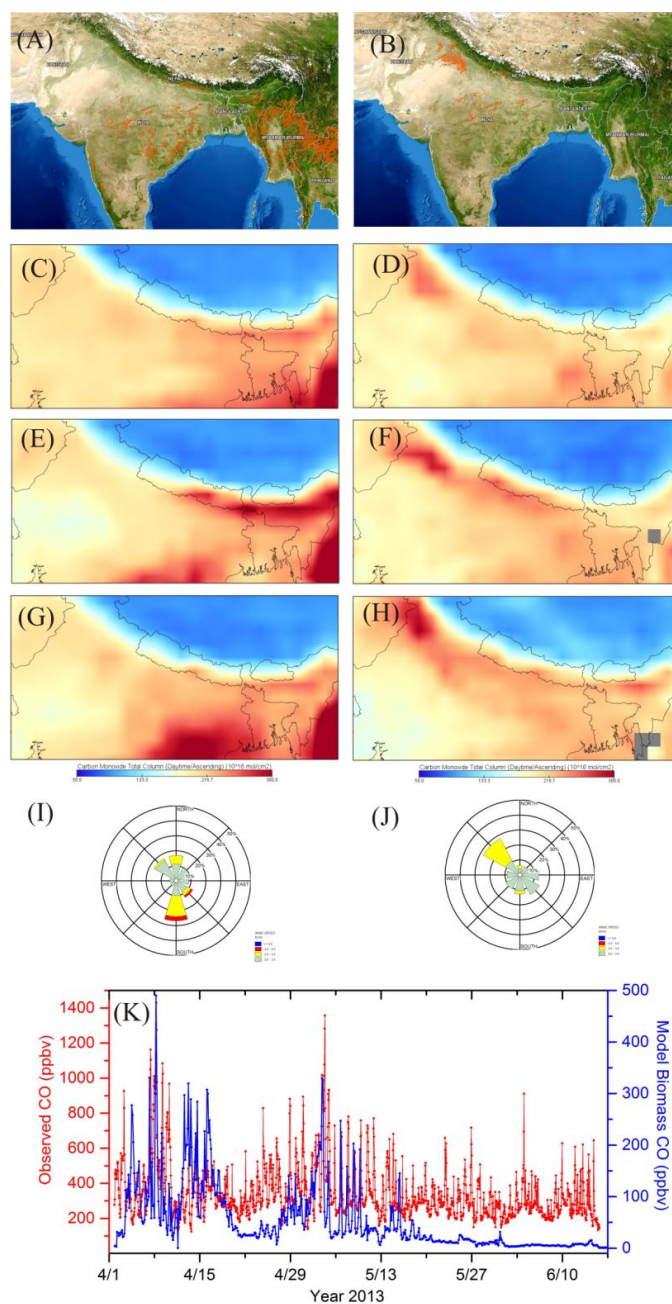
852 **Figure 8.** Diurnal variation of the planetary boundary layer (PBL) height at Lumbini obtained  
853 for every three hours of each day from the WRF-STEM model for the sampling period. The  
854 square mark in each box represents the mean PBL height, bottom and top of the box represents  
855 25<sup>th</sup> and 75<sup>th</sup> percentile, top and bottom of the whisker represents 90<sup>th</sup> and 10<sup>th</sup> percentile  
856 respectively.



857

858 **Figure 9.** Time series of daily average CO, BC concentration, absorption Ångstrom exponent  
859 (AAE), along with fire counts acquired with the MODIS instrument onboard TERRA satellite for  
860 a 200x200 km grid centered at Lumbini. Two rectangular green boxes represent two episodes  
861 with high peaks in CO and BC concentrations.

862



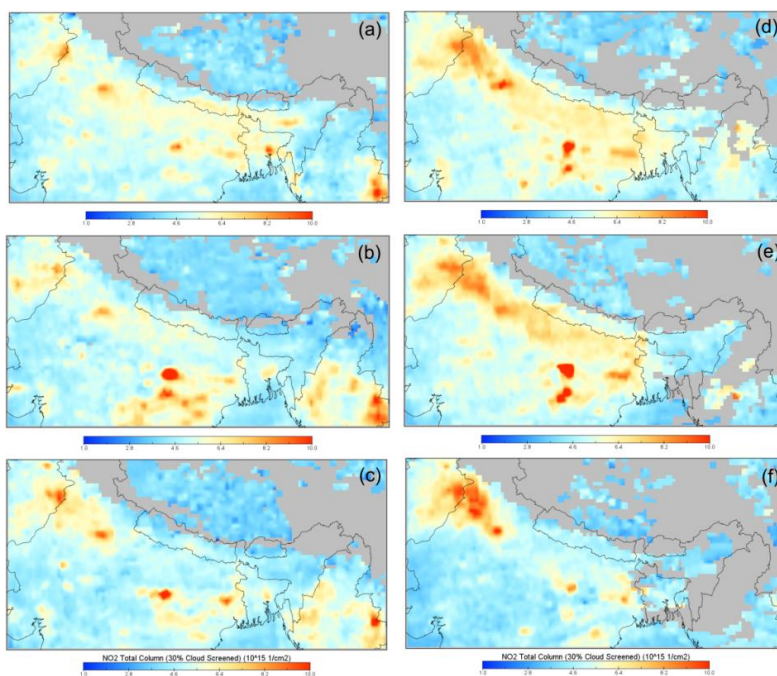
863

864 **Figure 10.** Active fire hotspots in the region acquired with the MODIS instrument on TERRA  
865 satellite during (A) Event-I (7-9 April) and (B) Event-II (3-4 May). CO emissions, acquired with



866 AIRS satellite, in the region 2 days before (3-5 April), during (7-9 April) and 2 days after (10-12  
867 April) the Event-I are shown in panels (C), (E) and (G), respectively while panels (D), (F) and  
868 (H) show CO emissions 2 days before (1-2 May), during (3-4 May) and 2 days after (5-6 May)  
869 the Event-II. Panels (I) and (J) represent the average wind rose plot of observed wind direction  
870 and wind speed during Event I and II, respectively. (K) Observed CO versus Model open  
871 burning CO illustrating contribution of forest fires during peak CO loading.

872

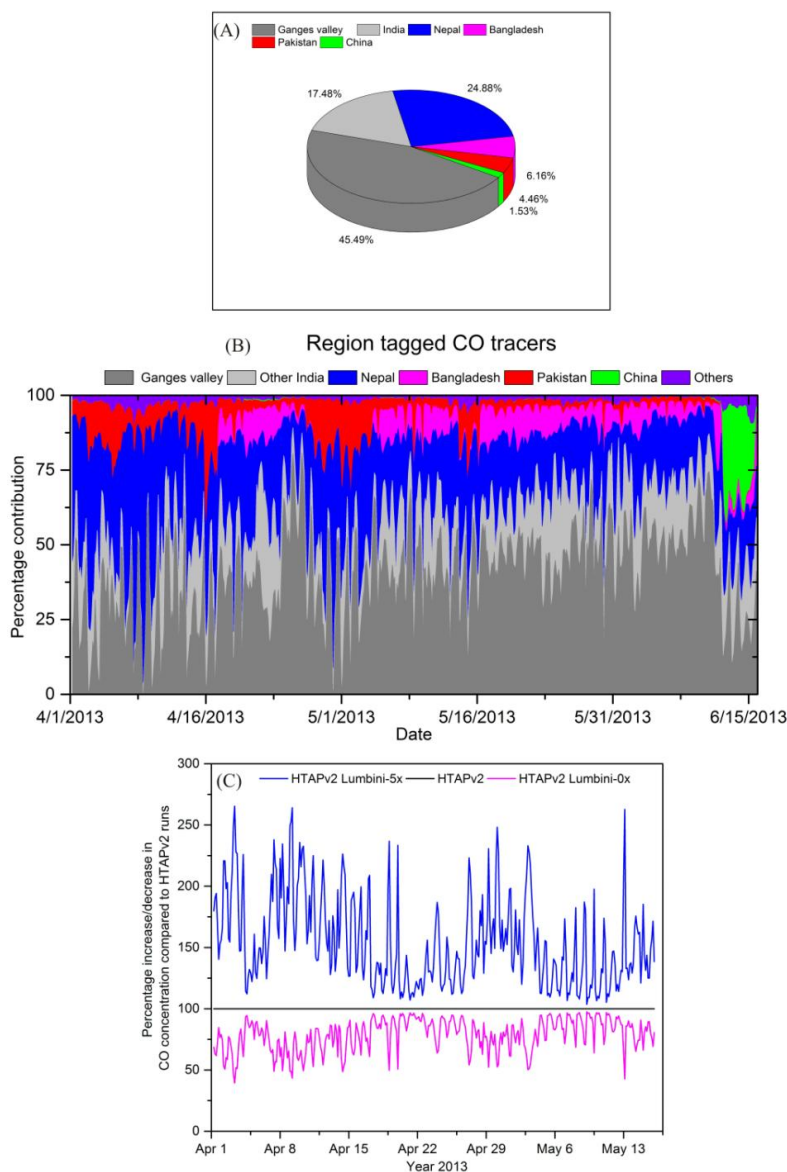


873

874 **Figure 11.** NO<sub>2</sub> total column obtained with OMI satellite over the region (a) before, (b) during,  
875 and (c) after the Event- I. The panels (d), (e), (f) show NO<sub>2</sub> total column before, during and after  
876 the Event- II.

877

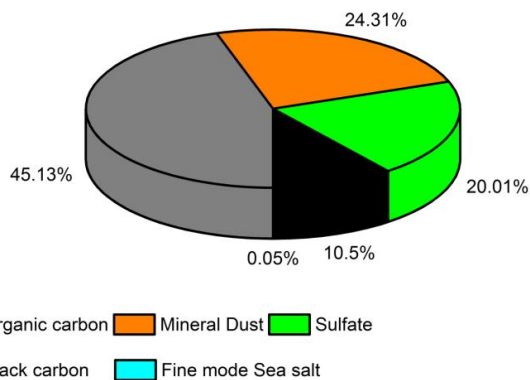
878



879

880 **Figure 12.** (A) WRF-STEM model estimated contributions of various source regions to average  
881 CO concentration in Lumbini for the sampling period, (B) time series of region tagged CO tracer  
882 during the whole measurement period using HTAP emission inventory and (C) Figure showing  
883 percentage increase/decrease in CO concentration with different emissions scenario.

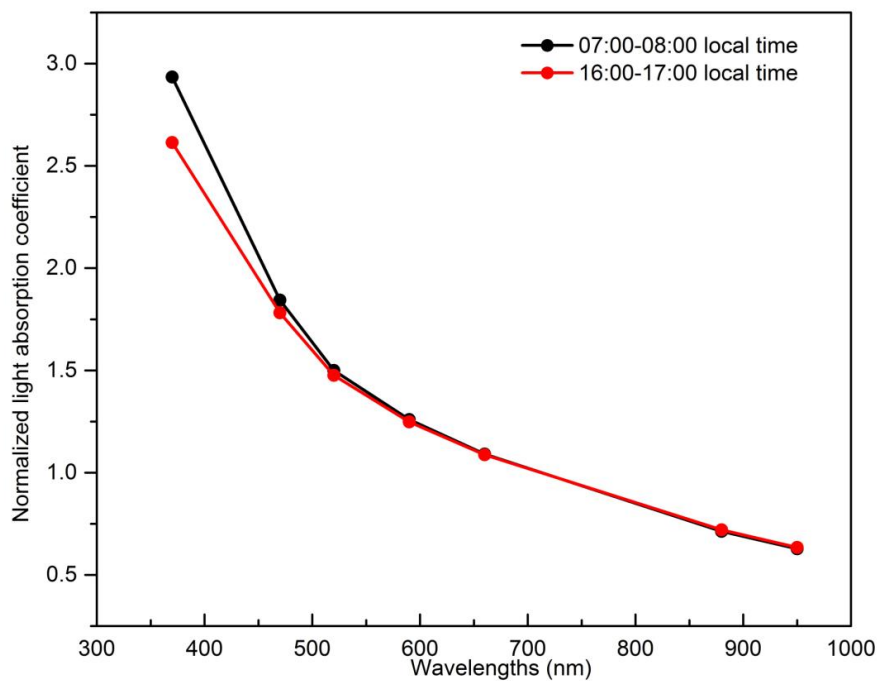
884



885

886 **Figure 13.** WRF-STEM model estimated PM<sub>2.5</sub> chemical composition at Lumbini for pre-  
887 monsoon season 2013

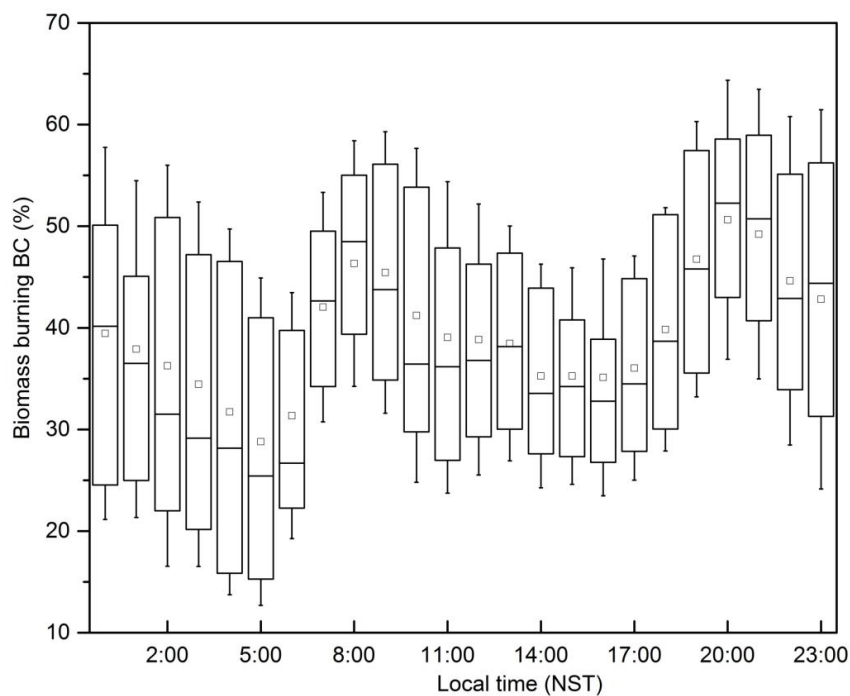
888



889

890 **Figure 14.** Normalized light absorption coefficients during cooking (07:00-08:00) and non-  
891 cooking (16:00-17:00) period based on diurnal variation of BC at Lumbini during the sampling  
892 period in premonsoon season 2013.

893



894

895 **Figure 15.** Diurnal variation of the fractional contribution of biomass burning to ambient BC  
896 concentration at Lumbini for the measurement period. In each box, lower and upper boundary of  
897 the box represent 25<sup>th</sup> and 75<sup>th</sup> percentile, respectively, top and bottom of the whisker represents  
898 90<sup>th</sup> and 10<sup>th</sup> percentile, respectively. The mid-line in each box represents median while the  
899 square mark represents the mean for each hour.